Chapter 18
Spaceborne Experiments

Roberto Battiston

18.1   Introduction: Particle Physics from Ground to Space

The Universe is the ultimate laboratory to understand the laws of nature. Under the action of the fundamental forces, lasting infinitesimal times or billion of years, matter and energy reach most extreme conditions. Using sophisticated instruments capable to select the signals reaching us from the depths of space and of time, we are able to extract information otherwise not obtainable with the most sophisticated ground based experiments. The results of these observations deeply influence the way we today look at the Universe and try to understand it.

During hundreds of thousands of years we have observed the sky only using our eyes, accessing in this way only the very small part of the electromagnetic radiation which is able to traverse the atmosphere, the visible light. The first telescope observations by Galileo in 1609, which dramatically changed our understanding of the solar system, yet were based only on the visible part of the electromagnetic spectrum. Only during the second half of the twentieth century we started to access wider parts of the spectrum. After the end of the war, using the new radar related technology, the scientists developed the radio telescopes to record the first radio images of the galaxy. But only in the 60's, with the advent of the first man made satellites, we began to access the much wider e.m. spectrum, including infrared, UV, X-ray and γ-ray radiation.

A similar situation happened with the charged cosmic radiation. Cosmic Rays, discovered by Hess in 1912 [1] using electrometers operated on atmospheric balloons, for about 40 years were the subject of very intense studies. The discovery of a realm of new particles using CR experiments, gave birth to particle physics

R. Battiston (✉)

Dipartimento di Fisica, Università di Trento, Povo, Italy
e-mail: roberto.battiston@pg.infn.it; roberto.battiston@unitn.it

823

and to high energy physics, successfully performed, since the 50's, at particle accelerators. However, the study of the cosmic radiation performed within the atmosphere, deals only with secondary particles. The primary radiation can only be studied with stratospheric balloons or using satellites. In 1958 Van Allen [2] and collaborators studied for the first time the charged cosmic radiation trapped around the Earth, and, since, the measurement of Cosmic Rays from space has become an important tool for the study of the Universe.

A third, more recent example is the discovery of ravitational waves (GW) [3], one hundred years after the prediction of Einstein [4]. Direct observation of gravitational waves opened a new era in astrophysics, adding to the spectrum of electromagnetic radiation the new messenger represented by GW. Since the pioneering attempts of Weber [5] in the 60's, using resonating bars, the GW community has developed in the 90's a network of $O(1)$ km arms, ground based interferometers to search for GWs in the frequency range 10 Hz to 100s of Hz [6],[7]. The detected signals confirm the prediction of General Relativity but also validate the sensitivity of the interferometer technologies. GW are expected much more abundantly in the frequency range $O(0.001)$ Hz to a $O(1)$ Hz. This range can be studied with a $5 \cdot 10^6$ km arm, space based interferometer, as the proposed ESA/NASA LISA mission. The successful LISA technology demonstrator, the ESA lead LISA-Pathfinder (LISA-PF) [8] flown in 2016, opened the way for the LISA[9] adoption, to be developed and implemented during the 20's to start operating at the end of the 20's or a the beginning of the 30's.

During the last century, particle detectors developed on ground have been adapted or designed to be used on stratospheric balloons and on space born experiments. Space, however, is a hostile environment and launching a payload is a very expensive endeavour. For these reasons, the design and the testing of a spaceborn detector requires particular care. In this chapter we deal with this topic.

We begin discussing the properties of the space environment from the upper atmosphere, the transition from the atmosphere to the magnetosphere and from the magnetosphere to the deep interplanetary space.

We then address the requirements for hardness and survivability of space born instrumentation.

We subsequently turn to the issue of manufacturing of hardware to be operated in space, with particular care to the issue of the space qualification tests.

We will also discuss modern spaceborne high energy radiation detectors, mainly from the point of view of the design characteristics related to the operation in space. We will make no attempt to cover the historical development or to cover low energy radiation instrumentation, in particular X-ray space borne detectors.

18.2   The Space Environment

18.2.1   The Neutral Component

Although there are some notable exceptions, a good fraction of scientific satellites which observe the different kinds of radiations emitted by the universe operate on LEO (Low Earth Orbit), namely between 200 and 2000 km from the Earth surface. Below 200 km the atmospheric drag dramatically reduces the lifetime of satellites, above 700 km the radiation environment, due to the Van Allen belts, becomes more and more hostile.

When operating close to the lower limit of LEO orbits, the external surfaces of the payloads are affected by the heat produced by the upper atmosphere drag and by the corrosion due to the presence of highly reactive elements such as atomic oxygen. Above ~600 km drag is sufficiently weak not to influence anymore the lifetime of most satellites.

Altitudes below ~600 km are within the Earth's *thermosphere*, the region of the atmosphere where the absorption of the solar UV radiation induces a fast rate of temperature increase with the altitude. At ~200–250 km the temperature of the tenuous residual atmosphere reaches a limiting value, the *exospheric temperature* ranging from ~600–1200 K over a typical solar cycle. The thermosphere temperature can also quickly change during the geomagnetic activity.

Atomic oxygen is the main atmospheric constituent from ~ 200–600 km, since it is lighter than molecular nitrogen and oxygen. Figure 18.1 shows the altitude profiles of atomic oxygen for different solar activities. Atomic oxygen plays an important role in defining the properties of LEO space environment. Since this form of oxygen is highly reactive, surfaces covered with thin organic films, advanced composites or thin metallized layers can be damaged [10]. Kapton, for example, erodes at a rate of approximately 2.8 μm for every 10^{24} atoms/m^2 of atomic oxygen fluence [11], with the fluence during a time interval t being defined as $F_0 = \rho_N v t$, ρ_N being the number density of atomic oxygen and v the satellite velocity. Chemical reaction involving atomic oxygen can in turn produce excited atomic states emitting significant amount of e.m. radiation, creating effects such as the *shuttle glow* which are interfering with optical instrumentation.

18.2.2   The Thermal Environment

From a thermal point of view a spacecraft orbiting around the Earth is exposed to various heat sources; direct sunlight, sunlight reflected off the Earth or other planets (*albedo*) and infrared radiation emitted by the planet atmosphere or surface. The spacecraft in turn loses energy by radiation to deep space, which acts as a sink at 2.7 K.
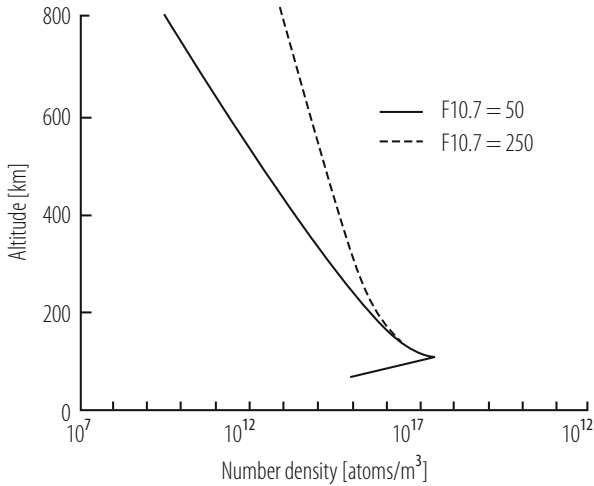
Fig. 18.1 Altitude profiles of number density of atomic oxygen at solar minimum (solid line) and solar maximum (dashed line) [12]

18.2.2.1 Direct Sunlight

A main source of thermal energy is of course the Sun, which acts as a black body at a temperature of 5777 K. The Sun is a very stable source of energy: at the Earth the energy flux varies from 1414 W/m^2 during winter time to 1322 W/m^2 during summer time. The mean intensity at 1 AU is called *solar constant* and is equal to 1367 W/m^2. The spectral energy distribution is approximatively 7% UV, 46% visible and 47% near-IR.

18.2.2.2 Albedo

Albedo refers to the sunlight reflected by a planet. It is highly variable with the conditions of the surface. For spacecraft orbiting close to the Earth, the *albedo* can reach a significant fraction, up to 57%, of the Earth emitted radiation, which in turn is 200–270 W/m^2, depending on the latitude and of the orbit inclination. The Earth itself is a blackbody radiating at around 255 K. This energy cannot be reflected away form the spacecraft which is approximatively at the same temperature. This energy can only be rejected through the spacecraft thermal control system. It is a non negligible amount of radiation: for example, when the Shuttle bay area looks at the illuminated surface of the Earth, its temperature reaches values close to 250 K even if the back of the spacecraft sees the 2.7 K of deep space.

18.2.3   The Charged Component

18.2.3.1   The Low Energy Plasma

At typical Shuttle altitudes, $\sim$300 km, about 1% of the atmosphere is ionized. This fraction increases to 100% at geosynchronous altitudes. This plasma environment can easily charge up satellite components, both on the surface and on the interior of the spacecraft. If the charging exceeds the electric breakdown and discharges are produced they can damage the satellite electronics. The charged component of the radiation is heavily influenced by the existence of the Earth magnetic field. The Earth magnetic field is roughly dipolar:

$$B(R, \theta) = (1 + \sin^2 \theta_M)^{1/2} B_0 / R^3 \qquad (18.1)$$

where B is the local magnetic field intensity, θ_M is the magnetic latitude, R is the radial distance measured in Earth radii (R_E) and B_0 is the magnetic field at the equator and at $R = 1$, $B = 0.30$ G. The interaction between the solar wind and the Earth's magnetic field results in a magnetic field structure much more elongated on the night side than it results on the day side, known as *magnetotail*. The resulting magnetic structure is called *magnetosphere* (Fig. 18.2).

The electrical potential of a spacecraft or payload is measured with respect to the nearby plasma when the net charge flow is zero. This current is the sum of the various exchanges of charge between the plasma and the spacecraft including photo-extraction and secondary emission from the spacecraft surfaces. The single
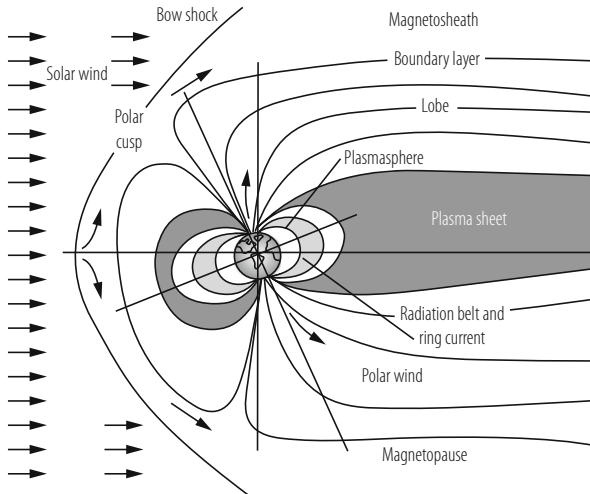

Fig. 18.2 Cross section of the Earth's magnetosphere, showing the key plasma and energetic particle populations [12]

component voltage to the spacecraft ground depends on the element capacitance to the nearby materials. Space charging is particular detrimental in orbits where electron energies in the 10 to 20 keV range dominate the current from the plasma to the spacecraft. At low altitudes this happens only at high latitudes where there are energetic auroral electrons [13]. At other low altitudes locations, low energy electrons are sufficiently abundant to keep the electric fields below the breakdown levels.

The situation is different in higher orbits, such as geosynchronous, where surface charging occurs during magnetospheric substorms between the longitudes corresponding to midnight and dawn [14]. The design of spacecrafts capable to keep a small differential potential with respect to the plasma or to tolerate electrostatic discharges is necessary for these orbits. Design rules and material selection criteria have been developed to help reducing the effect of surface charging on spacecrafts and payloads [15, 16].

It should be noted that, although in the equatorial regions of LEO differential charging is small, the potential of the spacecraft with respect to the surrounding plasma can reach a level close to 90% of the solar array voltage. This should be taken into account when designing experiments aimed to study the plasma properties or when dealing with high voltage power supplies.

18.2.3.2   The Trapped Radiation

Well inside the magnetosphere lie the radiation belts, regions where energetic ions and electrons experience long-term magnetic trapping [17]. Since this trapping requires stable magnetic fields, near the magnetopause the magnetic field fluctuations induced by solar wind prevent long term trapping. On the low altitude side the atmosphere limits the radiation belts to the region above 200 km. The magnetic geometry limits the trapping volume to magnetic latitudes of about 65°. A *magnetic L − shell* is the surface generated by rotating a magnetic field line around the Earth dipole axis and L is measured in units of Earth radius. Trapped particles spiral along paths centered on a given shell. The shell surface can be approximately described as: $R = L \cos^2 \theta_M$ [18]. Electrons preferentially populate the toroidal region centered on $L \sim 1.3$ (inner zone) while protons populates the region around $L \sim 5$ (outer zone). The energy of these trapped particles is greater than 30 keV and can reach hundreds of MeV. The intensity of the trapped radiation flux can reach the maximum intensity of $10^8 - 10^9 \, \text{cm}^{-2} \, \text{s}^{-1}$ at a distance of $\sim 2 \, R_E$ for $E_k > 0.5$ MeV electrons and of $\sim 3 \, R_E$ for $E_k > 0.1$ MeV protons. Satellite components, in particular electronics, can be damaged by this penetrating charged form of radiation. A dramatic example of this occurred in 1962 when several satellites ceased to operate after their solar cells were damaged by the increase of radiation belts intensity from high altitude nuclear explosions. Since the basic principles of the trapping are well understood, radiation belts can be modeled quite accurately: a standard model of the Van Allen Belts is available by the National Space Science Data Center [20]. It should be noted, however, that due

to the structure of the Earth magnetic field, which has a dipolar structure not aligned with the Earth angular momentum, the radiation belts are only approximatively of toroidal shape: in the vicinity of the South Atlantic, the structure of the belts is strongly affected and the bouncing altitude of the trapped particles decreases very significantly (South Atlantic Anomaly, SAA). This leads to a region which, although located at LEO altitudes, is characterized by a very intense particle flux, since it is basically within the belts.

Energetic particles, such as electrons from 200 to 1.5 MeV, can implant in the dielectrics and produce discharges within the components themselves (*bulk charging*). At even higher energies, above few MeV, charged particles are highly penetrating and release their energy in the form of ionization deep inside materials. The damages induced by this penetrating radiation can be divided into:

- total dose effects which can degrade the material properties of microelectronics devices, optical elements (lenses, mirrors), solar arrays, sensors, . . .
- Single Event Effects or Phenomena (SEE or SEP), effects induced by single particles creating short circuits which can temporarily or permanently damage microelectronics components. They are further subdivided into

    – *Single Event Upset (SEU)* or *bitflip* which although do not damage the electronics may influence the operation of onboard software.
    – *Single Event Latch-up (SEL)*, causing sudden low resistance paths and subsequent drift on the power lines of electronics components which start to operate abnormally until the correct voltage is restored. Depending on the power supply performances SEL can be recovered or could cause permanent damages.
    – *Single Event Burnout* (SEB), causing permanent failures of electronic devices.

18.2.3.3   Solar Particle Events

The Solar Particle Events (SPE) occur in association with solar flares. They consist in an increase of the flux of energetic particles, mostly protons, ($\sim$1 MeV to $\sim$1 GeV) over time scales of minutes, lasting from few hours to several days. Although SPEs occur at a rate of few per year, they are very dangerous for payloads and astronauts, due to the intense radiation dose they deliver, several orders of magnitude higher than in normal conditions (see Fig. 18.3). The global time structure of a SPE is somewhat characteristic (see Fig. 18.4), although the detailed structure depends on the evolution of the original solar flare. X-rays reach the Earth within minutes together with the most relativistic part of the proton spectra; lower energy particles diffuse over time scales of several hours. The fast component of a SPE can be used as early warning to protect the most delicate parts of a payload by switching them off, by using radiation shields or changing the satellite attitude or operational mode.
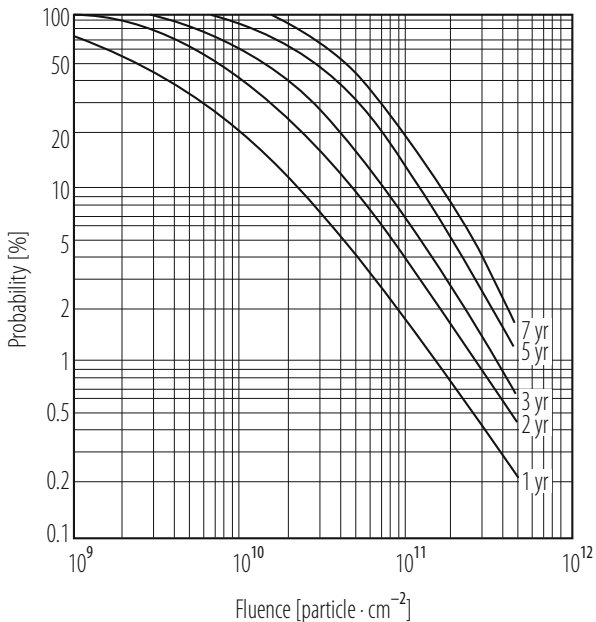
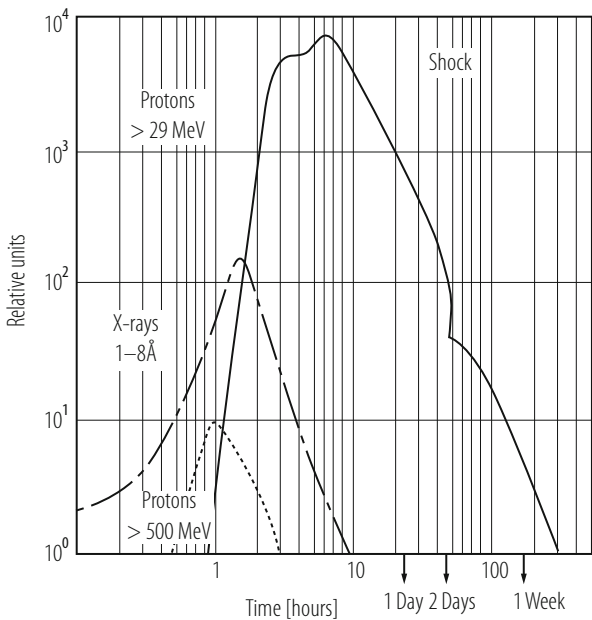**Fig. 18.3** Probability of exceeding a given fluency level as a function of mission duration [12]

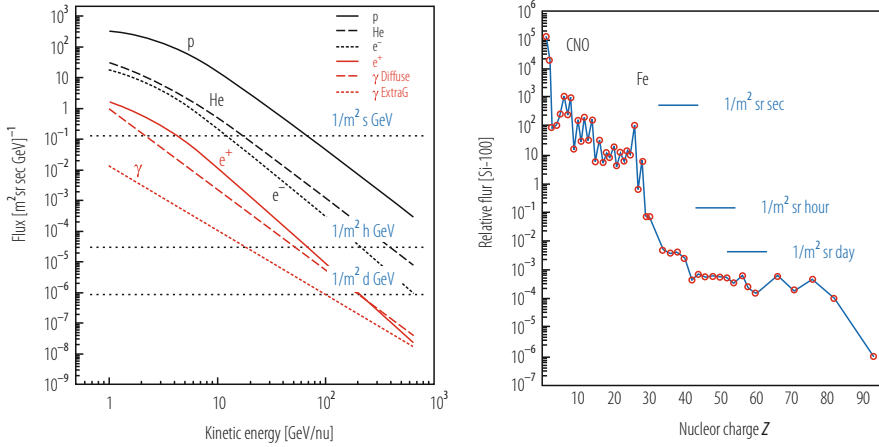**Fig. 18.4** Typical time evolution of a Solar Particle Event (SPE) observed from the Earth [12]

Fig. 18.5 Galactic Cosmic Rays Composition. Left, differential flux of H and He nuclei compared with e^-, e^+ and γ rays. Right, total flux of the nuclear component of galactic Cosmic Rays as a function of the electric charge Z

18.2.3.4 Galactic Cosmic Rays

Galactic Cosmic Rays (GCR) are high energy charged particles reaching the Earth from outside the solar system. The GCR composition is similar to the composition of the energetic particles within the solar system but extend to much higher energy (see Fig. 18.5 and Sect. 18.2.3.4). Their energy ranges from $O(100\,\text{MeV})$ to $10^6\,\text{GeV}$ or more, with an energy spectrum falling as $\sim E^{-2.7}$ for $E > 1\,\text{GeV}$. These particles are very penetrating, loosing their energy only by ionization. Nuclear interaction phenomena are indeed negligible in space for what concerns radiation damages. The ionization losses can create $SEEs$ as discussed above. $GCRs$ have a significant content of high Z particles, fully ionized nuclei with charge extending up to Iron ($Z = 25$). Since ionization losses are proportional to Z^2, high Z GCR can be very effective in causing $SEEs$.

18.2.4 Space Debris

Orbiting spacecraft are subjected to hypervelocity (several km/s) impacts with micron size or larger pieces of dust or debris, both of natural (*micrometeorites*) and artificial (*orbital debris*) origin. These impacts can have dramatic effects on a space mission. The probability of a catastrophic impact can be assessed for a given mission and payload. Some measures can be implemented to reduce the effect of the space debris protecting the most important parts with screens made of multilayered materials which can absorb and dissipate the energy of the incoming fragments.

18.3 Types of Orbits

The choice of the orbit heavily influences satellites and payload design.

Many scientific applications are operating on Earth-Referenced Spacecraft orbits. Depending on their typical altitude we talk of *Low Earth Orbits (LEO)*, which are mostly below the Van Allen Belts (typically below 1000 km of height), and of *Geosynchronous Orbits (GEO)* which are well above the Van Allen Belts. Payloads spending substantial time within the Van Allen belts are exposed to high doses of radiation and requires particular care designing and protecting the electronics from SEE and total doses effect.

Table 18.1 shows the types of specialized Earth-Referenced orbits.

Higher orbits are typical of interplanetary missions; for these missions the typical doses received by the satellite payloads are significantly higher than for LEO but lower than within the Van Allen Belts. Far away from the Earth satellites are not anymore shielded from $SPEs$ by the Earth shadow nor by the screening effect of its magnetic field. SEE due to heavy ions and low energy protons should be carefully taken into account when designing the payload electronics.

The space radiation environment remains one of the primary challenges and concerns for space exploration, in particular for deep space missions of long duration, i.e., when the the combined shield due to Earth magnetosphere and atmosphere vanishes. In the inner heliosphere, major sources of radiation are Galactic Cosmic Rays, Solar Particles and Jovian Electrons. Furthermore, in the space nearby Earth particles (mainly electrons and protons) are trapped within the Van Allen radiation belts. Particles populating such a space environment induce single event and cumulative dose in spacecraft materials and, eventually, create electronics hazards.

Table 18.1 Specialized Earth-Referenced orbits

Orbit	Characteristics	Application
Geosynchronous (GEO)	Maintains nearly fixed position over equator	Communication, weather
Sun-synchronous	Orbit rotates so as to maintain approximately constant orientation with respect to Sun	Earth resources, weather
Molniya	Apogee/perigee do not rotate	High latitude communications
Frozen Orbit	Minimizes changes in orbit parameters	Any orbit requiring stable conditions
Repeated Ground Track	Sub orbits repeats	Any orbit where constant viewing angles are desirable

18.4   Space Mission Design

18.4.1   The Qualification Program

Since repairing in space is extremely expensive, if at all possible, designing and building spacecraft and payloads which maximal reliability is a must in the field of space engineering. It follows that quality control is an essential part during the various phases of the program. The *Qualification Program* adds to the cost of the space hardware construction, sometime very significantly, but it makes sure that the program is not headed for failure.

Qualification tests must be designed and implemented to check that the spacecraft/payload can withstand the challenges of launch, deployment and operation in space. Subsystems and components environmental tests include vibration, shock and thermal vacuum, electromagnetic compatibility and radiation hardness.

Although the goal is the same, testing strategies are not unique. There are indeed various testing methods:

- *dedicated qualification hardware* (QM): a set of qualification components is built and tested at qualification levels. A set of flight components (FM) is then built and launched after passing a qualification test a lower levels;
- *proto − flight* approach: a set of flight components is tested at qualification level then assembled into a subsystem or payload which is tested at qualification levels and then launched;
- *similarity* approach: demonstrate that the components and the environment are identical to previously qualified hardware.

A typical test sequence includes a series of functional tests preceeding/following each environmental test, for example:

- functional test;
- vibration test (levels depending on the mission);
- functional test;
- shock test (levels depending on the mission);
- functional test;
- thermal-vacuum tests, including some functional tests during exposure;
- Electro Magnetic Compatibility (EMC) tests (if required);
- flash X rays with functional tests during exposure (if required);

18.4.2   Vibration and Shock Test

A payload must withstand vibrations caused by the launch vehicle and transmitted through its structural mount. During launch, payload components may experience shocks due to the explosives used for the separation of the various stages. In case reentry is foreseen, they do experience shocks when entering the atmosphere as

well as during the landing phase. In order to understand the dynamical behavior of the payload and of its mounting under these circumstances, Finite Element Analysis (FEA) dynamic and numerical analysis together with Computer Aided Design (CAD) simulation should be performed. In this way it is possible to search for resonances of the mechanical structures, identifying conditions where the material could be stressed or damaged. Following an iterative process the mechanical design of the payload and of its mountings can be improved until all negative margins are eliminated. Dynamic and vibration tests are then performed on a qualification model, using for example an electro-dynamical shaker operating at frequencies between 5 and 3000 Hz, with a spectrum which depends on the mission characteristics. Table 18.2 shows a typical acceleration spectrum expected for payload launched using the Shuttle transportation system. Qualification levels are typically higher by factor 2 to 4. Shock tests are performed using a similar strategy. For example Fig. 18.6 shows shock levels used to simulate the launch of an Alpha-Centaur rocket.

Table 18.2 Maximum expected flight levels for a shuttle mission

	Frequency range	Frequency dependence
X axis	20–58 Hz	0.0025 g^2/Hz
	58–125 Hz	+9 dB/Octave
	125–300 Hz	0.025 g^2/Hz
	300–900 Hz	−9 dB/Octave
	900–2000 Hz	0.001 g^2/Hz
Overall = 3.1 Grms		
Y axis	20–90 Hz	0.008 g^2/Hz
	90–100 Hz	+9 dB/Octave
	100–300 Hz	0.01 g^2/Hz
	300–650 Hz	−9 dB/Octave
	850–2000 Hz	0.001 g^2/Hz
Overall = 3.1 Grms		
Z axis	20–45 Hz	0.009 g^2/Hz
	45–125 Hz	+3 dB/Octave
	125–300 Hz	0.025 g^2/Hz
	300–900 Hz	−9 dB/Octave
	900–2000 Hz	0.001 g^2/Hz
Overall = 3.1 Grms		

18.4.3 Environmental Tests

The environmental qualification campaign of a space component can be divided into three main steps. The first step consists in the development of requirements and constraints related to the payload and to the mission. The second step is
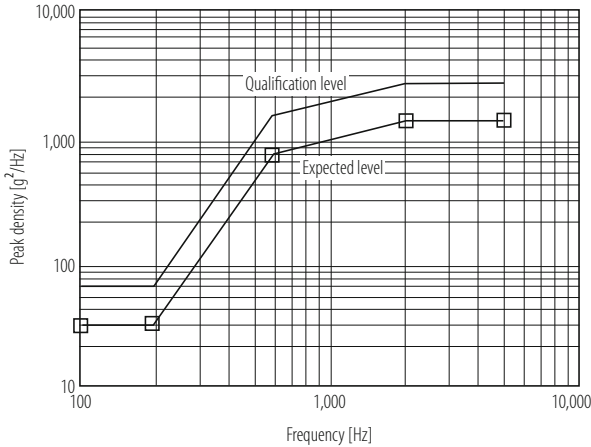
Fig. 18.6 Shock levels simulating the launch environment of an Alpha-Centaur rocket: qualification levels are designed to be greater than the expected design values [12]

to determine and define the space environment (in terms of temperatures, heat transfer ways, worst hot and cold case, etc.) that will characterise thermal conditions throughout the entire life of the component. An important part of the process of qualification is then the thermal analysis which can be conducted using FEA techniques. Once an acceptable thermal model has been developed, test predictions can be calculated to correlate thermal verification tests with the test results. If this correlation is found acceptable, the thermal model is then used to perform flight predictions. If, instead, the correlation is poor the thermal analysis and the hardware configuration need to be carefully checked to understand whether the actual configuration (hardware) requires modifications or the thermal model needs to be updated. Payload temperature requirements derive from the spacecrafts thermal design and the orbital environment and attitude. The purpose of these tests is to demonstrate that the subsystems comply with the specification and perform satisfactorily in the intended thermal environment with sufficient margins. The test environment should be based either on previous flight data, often scaled for differences in mission parameters, or, if more reliable, on analytical prediction or by a combination of analysis and flight data. A margin can include an increase in level or range, an increase in duration or cycles of exposure, as well as any other appropriate increase in severity of the test. Humidity and thermal qualification tests in climatic rooms are performed to test the behaviour of the electronic components and mechanical structures under thermal and humidity changes. The tests are conducted using climatic chambers, with temperature ranges depending on the mission parameters: for a LEO mission typical range lays within $-80\,^{\circ}$C and $+120\,^{\circ}$C for a planetary mission wider intervals are required. Components should be switched on and work both at temperature extremes or during transition, following the mission specifications (see Fig. 18.7).
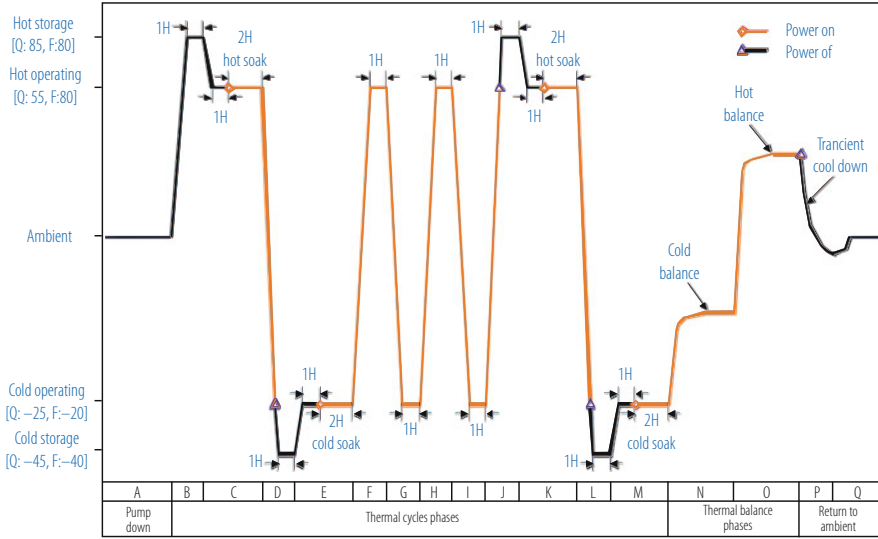
Fig. 18.7 Typical Thermal Vacuum Cycling test profile for a payload to be operated on a LEO orbit on the ISS [54]

18.4.4 EMC Tests

Another area where space payloads are submitted to extensive testing is the compatibility to Electro Magnetic fields, either radiated or received. During the test of radiated EM the device under test is powered and operated in standard operating condition in an EM anechoic chamber. Through suitable antennas and filters read by receivers, the intensity of the emitted radiation is measured as a function of the frequency. The results are compared with the limits requested by specific standards or design rules. If the limits are exceeded, then the electrical grounding or design of the device should be modified. During the received EM test, the device is operated within an EM anechoic chamber while EM radiation, monochromatic or with a specific spectral structure, is generated at a predetermined intensity using special antennas located nearby. The purpose of the test is to check that the item under test does not exhibits anomalies when illuminated by beams of EM radiation, typically emitted by a communication antenna or a nearby electronic device. Figure 18.8 show a typical the result for an EMC radiated test on a payload to be operated on the ISS.

18.4.5 Radiation Hardness Tests

As discussed in the previous paragraphs, the space environment is particularly harsh for operating microelectronics devices, due to the presence of single, heavily
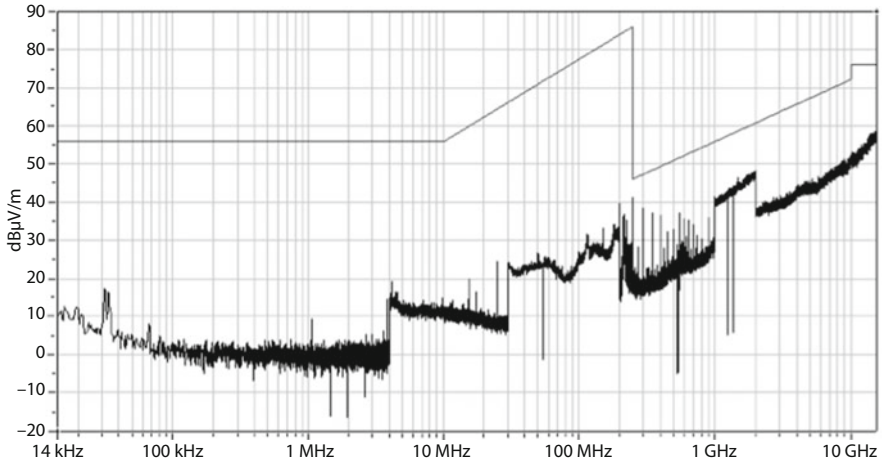
Fig. 18.8 Typical radiated EMC tests result for a payload to be operated on a LEO orbit on the ISS [19]. The thin line presents the e.m. field limits which should not be exceeded as described in Table 18.3

Table 18.3 Radiated EMC limits for the tests described in Fig. 18.8

Frequency range	Emission [dBμV/m]	Antenna
14 kHz–10 MHz	56	rod—vertical
10 MHz–259 MHz	56–86 (16 dB/decade)	biconical—horiz/vert
259 MHz–10 GHz	46–72 (16 dB/decade)	double ridge—horiz/vert
10 GHz–20 GHz	76	horn—horiz/vert

ionizing particles which can deposit large amount of charge in the bulk, inducing short circuits or spurious currents in the solid state circuits. The total dose collected during a space flight is relatively small, mostly in the *krad* range, so the radiation damages are mostly due to Single Event Effects (*SEE*).

Depending on the type of circuits and on their construction technology, the sensitivity to ionizing radiation can be very different. In order to select families of commercial circuits which are more insensitive than others it is necessary to run testing campaigns, comparing the behavior of several different chips when exposed to low energy ion beams. The type circuits which shows *latch up* sensitivity or abnormal behavior only at high Linear Energy Transfer (*LET*) are the one which are radiation hard and can be used in space. In order to ensure statistical significance of the radiation hardness measurement, several chips of each type should be tested (typically > 5).

Often, it is possible to protect the circuit by limiting the current which can flow through the power lines, by the use of an active switch which temporarily cut off the voltage to stop the *latch up* effect. In order to develop and implement a protection scheme it is then important to understand which area of the chip is sensitive. Nowadays it is also possible to perform in laboratory part of these test

by mean of IR laser beams which are absorbed by the silicon and can deposit a controlled amount of energy into the bulk simulating the charge released by a low energy ion [21].

All microelectronics components used in a space experiment must be radiation hard. In addition, the design of the on board electronics should include multiple redundancy since the radiation damage due to SEE is a stochastic process.

Space qualification of radiation resistant devices for a mission not only requires the understanding of damage mechanisms [22], but also the knowledge of local particles (and species) intensities [23, 24] and, in addition, of dose amounts, deposited via ionization and non-ionization energy loss (NIEL) processes. The latter mechanism is that one responsible for displacement damages particularly relevant for semiconductor devices. Only recently, the SR (screened relativistic) NIEL treatment framework has allowed a comprehensive calculation of NIEL doses imparted by electrons, protons, ions and neutrons in any material and compound [25]. SR-NIEL treatment is currently embedded in ESA transport codes, like GRAS [27] and MULASSIS [28] as well as in GEANT4 and it is available at the SR-NIEL and SPENVIS websites.

18.5   Design of a Space Particle Detector

Space born radiation detectors for a space application are, in most cases, adaptation to the space environment of detection techniques used at accelerators or nuclear laboratories.

The environmental conditions discussed in the previous sections obviously influence the detectors design. Particularly important examples are the design of a controlled temperature environment and, for gas detectors, the establishment of controlled pressure conditions.

However, a space born particle experiment has specific limits of different nature which are basically not existing in the case of a laboratory experiment. They are:

- *Weight*. Each kg transported in orbit is very expensive in terms of propellent, costing from 10.000 to 50.000 €/kg, depending on the size of the satellite and orbit of deployment (larger satellites cost less than smaller satellites per kg, higher orbits cost more than lower orbits per kg). This is a substantial limitation for the size of a payload. In addition today space transportation systems have a maximum capacity of about 10 to 20 t in LEO;
- *Power*. The basic source of power in space is the solar energy transformed into electrical power by solar panels. The power can be accumulated in batteries for the periods of the orbit where the spacecraft is shadowed by the Earth. The amount of power consumed by a payload is thus proportional to the area of the panels. One kW of power in space is a large amount of energy consumption. For instance, the entire International Space Station (ISS) power capability does not exceed 110 kW.

- *Volume*. The largest transportation systems can carry payloads which must fit within a cylindrical volume having a maximum radius of about 3 m and a maximum length of about 10 m. Most particle detectors have much smaller sizes. Once in orbit, the size of the payload can increase very significantly, when solar panels, mirrors or radio antennas are expanded from the launch configuration.
- *Accessibility*. Because of the huge cost involved, most of the payload are not accessible during their lifetime in space. Very rare exceptions are the Hubble Space Telescope and the ISS. It follows that the reliability of the instrumentation is essential.
- *Consumables*. Due to the reasons listed above, the amount of consumables is limited. If consumables are needed, e.g. gas for a wire detector or cryogenics for a low temperature payload, the lifetime of the instrument will be limited. In orbit servicing is being developed nowadays for refurbishing the most expensive satellites, but it is still an emerging technology.

These limitations require the ingenuity of the scientist and the knowledge of the engineers to developed most advanced detectors within the available resources.

The reduction of weight calls for the most advanced techniques of CAD (Computer Aided Design) and FEA (Finite Element Analysis) to design structural elements which minimize the amount of material used while tolerating the mechanical stresses and shocks with margins of safety of 2 or more. The techniques used here are typical of aeronautics. The use of light advanced structural materials is mandatory e.g. aluminum, carbon fiber and in general composite materials. Once the structural properties are well defined, static and dynamic FEA is used to identify which part of the structure contribute to the weight without contributing to the structural properties. These parts are normally machined away during the construction. With the advent of Computer Additive Manufacturing (CAM) the weight optimization of structural elements and the integration of functional&structural elements is developing quickly to the advantage of the reduction of the mass of new payloads.

The reduction of power consumption calls for low power electronics and motors. The low power requirement is typical of consumer portable electronics. For this reason modern space experiments make extensive use of electrical devices (VLSI chips, actuators, motors,...) used in commercial applications. *Uprating* these parts to be used in space must be a part of the qualification process, in particular from the point of view of radiation hardness, which is not a requirement for consumer electronics. This approach of using $COTS$ (Component Off The Shelf) can reduce significantly the cost of a payload while producing very performant space instrumentation.

Due to the limited accessibility, reliability is a must in space born instrumentation. Reliability is the result of design, manufacturing, integration techniques which must be implemented since the early phases of the development of a payload. During the design phase, redundancy must be implemented in particular in the most critical areas. Special software allows, for example, to measure the probability of the failure of a given circuit, starting from the failure probability of its different components.

Typically the overall probability for a catastrophic failure must be in the range of 1% or less. Single point failures, namely parts of a circuit which are so critical that their failure would generate unacceptable level of malfunctioning, must be avoided. Redundancy of mission critical elements should at least be three to four fold. Similar techniques are applied to test the on board software, exploring all possible software states so to avoid unexpected software conditions which might degrade the payload performances. During the manufacturing phase and integration phases particular care should be given to Quality Assurance (QA), to ensure that the quality of the workmanship of the flight and qualification units and of the fully integrated payload matches the requirements of space standards and specifications. During the testing and qualification campaigns, all possible conditions to be encountered by the payload are simulated to make sure it will operate correctly under any circumstance. QA requires the operators to follow procedures written in advance, perform special tests and report all results and anomalies through written documents which can be verified and used by all the people involved in the various phases of development, commissioning and operation of the payload.

18.6   Space Borne Particle Detectors

The development of modern particle space borne detectors (both for charged particles and photons) has been preceded/accompanied by decades of development of particle detectors for ground based nuclear and particle physics detectors, followed by extended use on stratospheric balloons [29–38].

Small particles detectors have been routinely used on satellites mission to explore the Earth magnetosphere and heliosphere [39, 40].

Modern particle experiments in space can be grouped in three broad categories: (1) experiments measuring the composition, rates and energy spectra of the charged component, (2) experiments detecting single energetic photons and (3) interferometers designed to measure Gravitational Waves in space.

In the first category we find various types of magnetic spectrometers, in the second experiments are based on high granularity tracking calorimeters while the third category cover multiple arms laser interferometers. In the following paragraphs we will briefly discuss some of the most significant space particle detectors developed during the last 10 years, namely AMS-01/02 [41, 42] and PAMELA [43] for the charged component Agile [44] and Fermi [45, 46], for the electromagnetic component and LISA-PF[8] for measuring GW. We will underline the main differences with their ground based counterparts currently used at accelerators experiments. Details of the detection principles, readout electronics or on board software will not be given since they have been addressed in other chapters of this book.

18.6.1 *Magnetic Spectrometers*

The purpose of a space borne particle detector is to identify the basic properties of the charged cosmic radiation, namely its composition, the energy spectra of the various components and the corresponding fluxes. Thus, the components of a space born magnetic spectrometer are very similar to modern ground based spectrometers, namely:

- a magnet, permanent or superconducting, to measure the sign of the charge by bending the particles path;
- a precise tracking device to measure the particle signed rigidity ($R = B\rho = pc/Ze$), where B is the magnetic field and ρ is the radius of curvature;
- a scintillator based system to trigger the experiment and measure the Time of Flight;
- particle identification (ID) detectors like:

    - Transition Radiation Detectors (TRD) to separate e^+ and e^- from hadrons;
    - Cherenkov Ring Imaging detectors to measure the absolute value of the charge, Z, and the velocity;
    - Electromagnetic Calorimeters to identify the electromagnetic component within the cosmic radiation and measure its energy;
    - Neutron Counters to improve the calorimetric rejection the hadronic CR component.

The first magnetic spectrometers were flown on stratospheric balloons in the 80's. The magnets were based on superconducting coils. The magnets where switched on ground and operated cryogenically for a period of order of 1 day [29, 31–34]. Recently balloon cryostats were able to operate for order of few weeks making possible Long Duration Balloon flights (LDB) around the South Pole [35–38]. Pressurized stratospheric balloons are also beginning to operate Ultra Long Duration Flights (ULDB) which could eventually reach several months duration [90].

The first space borne large magnetic spectrometer, AMS-01 [41] was built only in the mid 90's, due to difficulty of developing a large magnet to be used in space. AMS-01 was the precursor flight of the AMS-02 spectrometer [42], approved by NASA to be flown to and operated on the international space station. (ISS): the engineering model, AMS-01, was operated during the 12 days Shuttle STS91 mission in June 1998 [47]. AMS-02, initially was based on a superconducting magnet to be installed on the ISS in the early 2000's, to be operated for about 3 years, namely for the estimated duration of the superfluid Helium consumable, with the possibility to be reflown after Helium refilling on Earth. The 2003 Challenger disaster forced the earlier retirement of the Shuttle fleet and a modification of the AMS-02 manifest: AMS-02 has been then flown to ISS in 2011 based again on a permanent magnet configuration to benefit of the longest possible exposure ensured by the ISS lifetime. In 2006 a smaller spectrometer, PAMELA [43] also based on a permanent magnet, was launched on a Resurs DK1 Russian satellite to operate in LEO.

One important difference between ground based or balloons magnetic spectrometers and the space borne version is related to the issue of the coupling between the Earth magnetic field and the magnet dipole moment. Since the payload attitude is not a relevant parameter for balloon spectrometers, superconducting magnets exhibiting significant dipole moment can be operated without problems. In space the situation is completely different: the magnetic coupling would affect the attitude of the entire satellite or platform, requiring continuous steering to keep a stable, outward looking attitude. It is then mandatory to design magnets having special geometries (see the following paragraph) and exhibiting minimal magnetic dipole moments.

18.7 Space Spectrometers Based on a Permanent Magnet

All space borne magnetic spectrometers which have been operated in space, AMS-01 (1998), Pamela (2006) and AMS-02 (2011) were based on permanent magnets.

18.7.1 The Alpha Magnetic Spectrometer on Its Precursor Flight (AMS-01)

AMS is an international project involving 16 countries an 56 institutes [42], operated under a NASA-DOE agreement, to install on the ISS a large magnetic spectrometer for the search of nuclear antimatter and to study the origin of dark matter. The first version of the spectrometer was built around a cylindrically shaped, permanent magnet having 800 mm of height and an inner diameter of 1115 mm, resulting in a geometrical acceptance of $0.82 \, \text{m}^2$ sr. Figure 18.9 shows the dimensions of the AMS-01 flight magnet. The magnet was made from 64 sectors. Each sector was composed of 100 $5 \times 5 \times 2.5 \, \text{cm}^3$ high grade NdFeB blocks. Figure 18.10 shows the arrangement of the field directions of the 64 sectors (left) and the resulting magnetic field map on the middle plane (right). This magnetic configuration is called *magic ring*, and ensures, theoretically, a small magnetic dipole field. To build this magnet the highest grade NdFeB available at the time was used, with an energy level of $(BH)_{max} = 50 \cdot 10^6$ GOe. This configuration resulted in an internal dipole field of 0.15 T and a negligible dipole moment. The total weight of the magnet including the support structure was 2.2 t. The magnetic field, directed orthogonally to the cylinder axis, provided an analyzing power of $BL^2 = 0.15 \, \text{Tm}^2$. Outside the magnet the field becomes less then 3–4 G anywhere at a distance larger than 2 m from the magnet center.

Before the construction of full scale magnets, many smaller magnets were built to confirm and measure the field inside the bore, the dipole moment and the flux leakage [41]. Three full scale magnets were built:
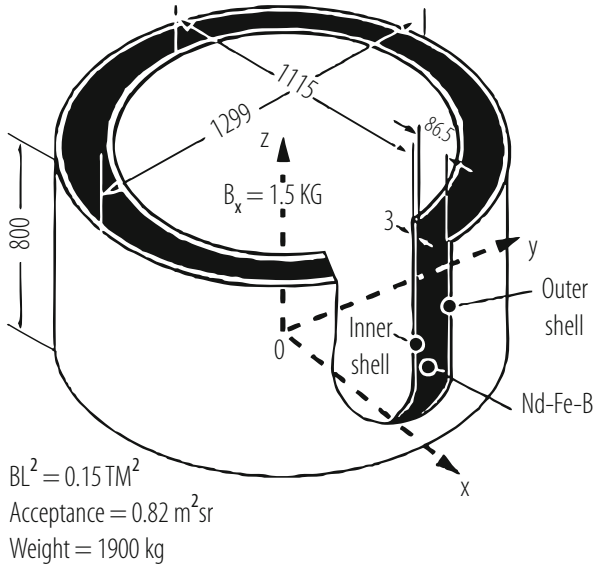
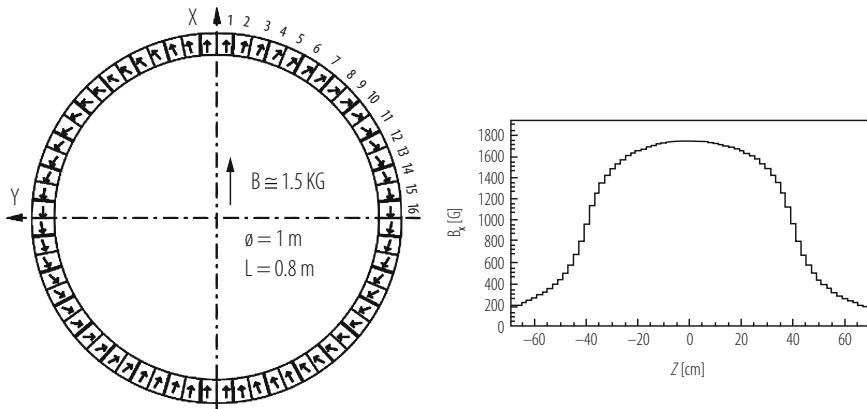**Fig. 18.9** Properties of the AMS-01 flight magnet (dimensions in mm)

Fig. 18.10 Magnetic field orientation of the AMS-01 magnet sectors (left); B_x field map along the vertical axis ($x = 0$, $y = 0$) (right)

(a) The first magnet was used in acceleration and vibration tests for space qualification.

(b) The second magnet was the flight magnet.

(c) The third magnet was built without glue for NASA safety tests.

The magnet, the supporting structure and space qualification testing were completed by the Institute of Electrical Engineering [48] and the Chinese Academy of Launch Vehicle Technology ($CALT$) [49]. Figure 18.11 shows the first magnet
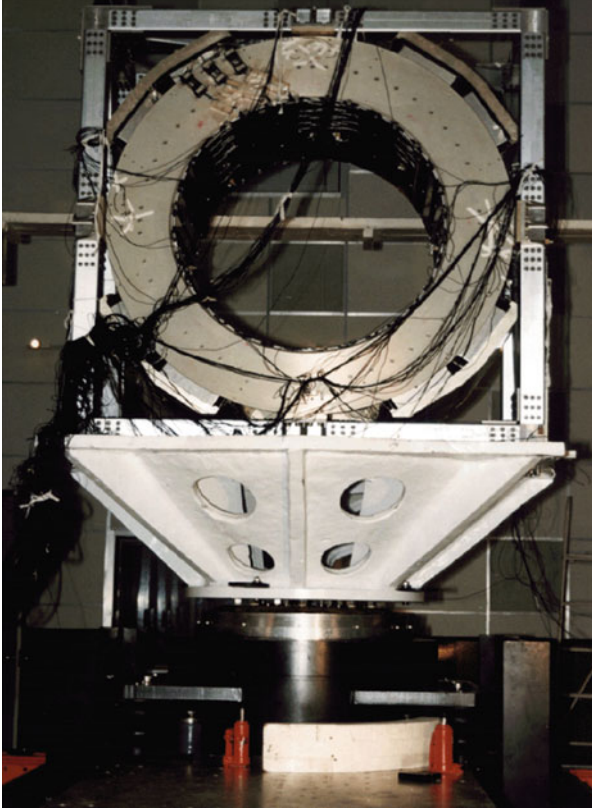
Fig. 18.11 AMS-01 magnet during vibration tests at the Beijing Institute of Spacecraft Environment and Engineering in Beijing, China

Fig. 18.12 AMS-01 magnet undergoing centrifuge (static load) testing at the Laboratory for Centrifugal Modeling in Beijing, China. The picture is blurred since it has been taking through a thick glass window
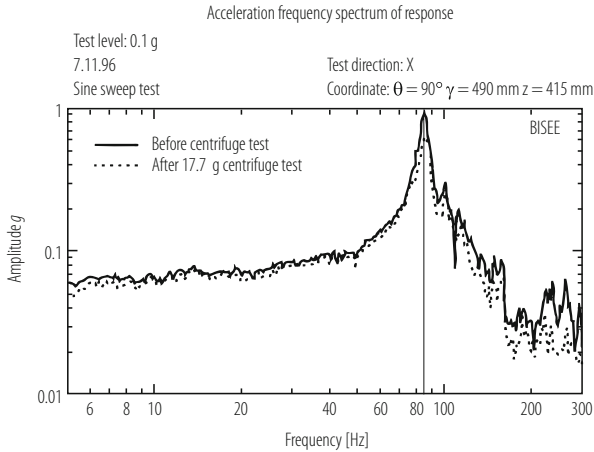
Fig. 18.13 Sine sweep test frequency spectrum response of AMS-01 magnet before and after 17.7 g centrifuge test

undergoing vibration testing. Figure 18.12 shows it undergoing centrifuge testing up to 17.7 g. Figure 18.13 shows the comparison of the sine sweep test results before and after the 17.7 g centrifuge test. The test results indicate that there is no deformation in the detector before and after this test and that the eigenfrequency for the magnet is above the ∼50 Hz region, where the spectral power of the random vibrations produced by shuttle is the highest, as imposed by the NASA safety requirements. The third full scale magnet was built because of the lack of knowledge of the glue performance over an extended period in the space environment. This magnet without any glue was to be tested to destruction to ensure that AMS could be returned on the Shuttle to Earth even if the glue completely failed. The result of the test shows that even with stresses 310 times higher than expected according to analysis the magnet would not break.

During spring of 2006 a smaller but sophisticated magnetic spectrometer, Pamela was launched from Baikonur on a Resource DK Rocket and inserted on a LEO for a 3 years mission. The Pamela experiment is built by an INFN-led international collaboration, and it was launched and operated under an Italian-Russian agreement. The magnet consists of 5 modules of permanent magnets, made of a sintered NdBFe alloy, interleaved by 6 silicon detector planes. The available cavity is 445 mm tall with a section of $1.31 \cdot 10^5$ mm^2, giving a geometrical factor of 20.5 cm^2 sr. The mean magnetic field inside the cavity is 0.4 T, providing an analyzing power $BL^2 = 0.1$ Tm^2 resulting in a Maximum Detectable Rigidity of 740 GV/c, assuming a spatial resolution of 4 μm along the bending view [43]. The apparatus is 1.3 m high, has a mass of 470 kg and an average power consumption of 355 W. The layout of the magnet and the experiment is shown in Fig. 18.14.
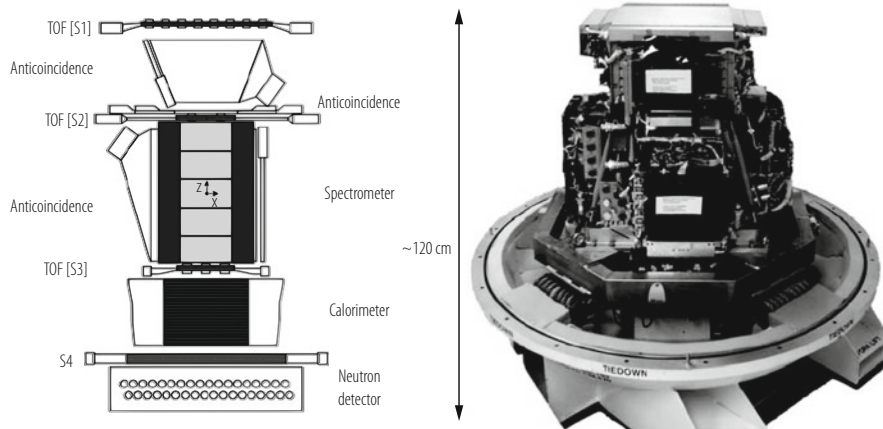
Fig. 18.14 Schematic lateral view of the PAMELA detector (left) and a photograph of it (right) taken before the delivery of the instrument for the integration to the Resours satellite. The geometrical acceptance of the detector is 20.5 cm^2 sr [63]

18.7.1.1 Superconducting Space Spectrometers

The sensitivity to new physics requires spectrometers able to explore higher Cosmic Ray energies while collecting large statistical samples. For this reason ground based modern spectrometers are routinely built using large superconducting magnets which measure particles with momenta in the multi-TeV range [50, 51]. It is of course much more difficult to design a superconducting magnet instead of a permanent magnet to be operated in space. Large facilities like the International Space Station could however provide the necessary infrastructure in terms of power, payload weight and size, data transfer and so on, to install and operate an superconducting spectrometer devoted to high energy particle physics in space. Already in the 80's a proposal was made to install on the Space Station a superconducting spectrometer, ASTROMAG [52]. ASTROMAG was designed around two parallel, large superconducting coils having opposite dipole moments, providing a highly non-uniform magnetic field but an almost zero residual dipole moment. The downsizing of the initial Alpha Station design which took place at the end of the 80's, put the ASTROMAG on indefinite hold status. In 1994 a new proposal was presented through DOE to NASA by the AMS Collaboration, to install and operate a large magnetic spectrometer on the ISS for at least 3 years. This proposal was based on a cylindrical magnetic geometry (*magic ring*), providing much more uniform magnetic field for the particle spectrometer and an almost zero magnetic dipole moment. After the successful flight of the AMS-01 permanent magnet in 1998, the AMS Collaboration proposed to DOE and NASA to upgrade the permanent magnet to a superconducting one having identical geometrical properties but an almost one order of magnitude stronger field (Fig. 18.15).
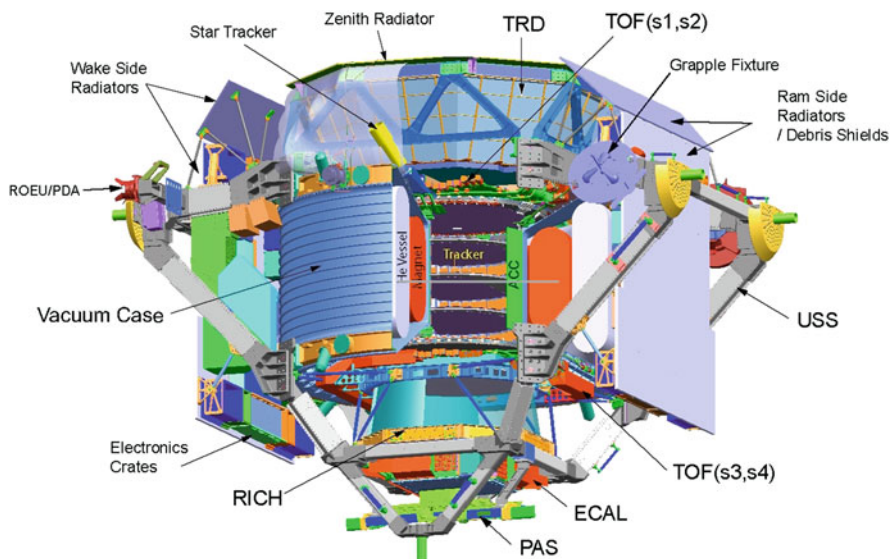
Fig. 18.15 Schematic 3D of the AMS spectrometer in the superconducting version

The project which developed during the years 2000–2010, consisted in the design, construction and extensive testing of the first space qualified superconducting magnet, including thermal-vacuum test in the large ESA-ESTEC space simulator in April 2010. In order to be compatible with the payloads designed for AMS-01, this magnet had identical inner dimensions to the AMS-01 permanent magnet, making the two magnet interchangable with the particle identification detectors. This fact has been instrumental to allow for the switch back to the permanent magnet when it became clear that the early retirement of Shuttle would not have allowed refilling of superfluid ^4He as initially planned. AMS-02 on a permanent magnet configuration has been largely benefitting of the longest possible exposure ensured by the ISS lifetime, which is particularly important in the search of ultrarare events (Fig. 18.16).

The AMS-02 superconducting magnet has been the first designed for operating in space. For this purpose a number of unique challenges had to be solved. Among them:

- endurance: how to maintain the magnet in the superconducting state for the longest possible time, of the order of 3 years, without cryogenic refill;
- safety: how to safely handle the large amount of energy ($O(MJ)$) stored in the magnet in case of a quench;
- mechanical stability: how to build a structure able to withstand large magnetic forces while being as light as possible.

Two magnets have been built. One is the flight magnet and the other is used for space qualification tests. The magnet system consists of superconducting coils, a

Fig. 18.16 The AMS-02 spectrometer during its integration at CERN in 2009 in the final flight configuration with the permanent magnet

superfluid helium vessel and a cryogenic system, all enclosed in a vacuum tank. The magnet operates at a temperature of 1.8 K, cooled by superfluid helium stored in the vessel. It was designed to be launched at the operating temperature, with the vessel full of 2600 liters of superfluid helium. Four cryocoolers operating between ∼300 and ∼80 K help to minimize the heat losses maximizing the endurance.

The magnet was designed to be launched with no field since it would be charged only after installation on the ISS. Because of parasitic heat loads, the helium will gradually boil away throughout the lifetime of the experiment. After a projected time of 3 years, the helium would be used up and the magnet would warm up and be no longer be operable. Three years of operation in space would indeed correspond to a continuum heat load into the superfluid Helium of about 100 mW, quite a small amount for a magnet which has a volume of about 14 cubic meters.

The coil system consists of a set of 14 superconducting coils arranged, as shown in Fig. 18.17, around the inner cylinder of the vacuum tank. The coil set has been designed to provide the maximum field in the appropriate direction inside the cylindrical bore, while minimizing the stray field outside the magnet. As a result, with the bore geometry identical to the geometry of the AMS-01 magnet, AMS-02 with the superconducting magnet would have had a field almost one order of magnitude larger. A single large pair of coils generates the magnetic dipole field perpendicular to the experiment axis. The twelve smaller flux return coils control the stray field and, with this geometry, they also contribute to the useful dipole field. The magnetic flux density at the geometric centre of the system is 0.73 T. The superconducting wire was developed specifically to meet the requirements of the AMS cryomagnet [53]. The current is carried by tiny (22.4 μm diameter) filaments of niobium titanium (NbTi) which are embedded in a copper matrix, which
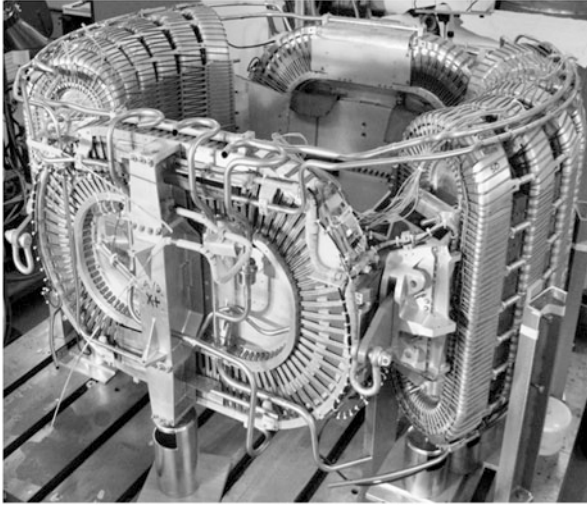
Fig. 18.17 The AMS-02 superconducting magnet: the dipole and the return coils are clearly visible, arranged in the characteristic cylindrical geometry

Table 18.4 AMS-02 superconducting magnet parameters

Parameter	Value
Central magnetic field B_x (at $x = y = z = 0$)	0.750 T
Dipole bending power	0.750 Tm^2
Maximum stray magnetic field at $R = 2.3$ m	13.2 mT
Maximum stray magnetic field at $Y = 2.3$ m	6.62 mT
Maximum stray magnetic field at $R = 3.0$ m	3.4 mT
Peak magnetic field on the dipole coils	5.75 T
Peak magnetic field on the racetrack coils	5.14 T
Maximum torque in geomagnetic field	0.237 Nm
Maximum stray magnetic field at $R = 3.0$ m	3.4 mT
Nominal operating magnet current	400 A
Stored energy	3.72 MJ
Nominal magnet inductance	48 H

is encased in high-purity aluminium. The copper is required for manufacturing reasons, but the aluminium is thermally highly conductive and much less dense, thus providing maximum thermal stability for the same weight. The characteristics of the AMS-02 superconducting magnet are listed in Table 18.4.

The current density in the superconductor is 2300 or 157 A/mm^2 including the aluminium. The 14 coils are connected in series, with a single conductor joint between each pair of adjacent coils. The magnet is designed for a maximum current of 459.5 A, although it is operated at ~85% of this value. The coils are not coupled thermally. All the coils are constantly monitored by an electronic protection system. If the onset of a quench is detected in any coil, heaters are powered in the other coils

to quench all 14 coils simultaneously. This distributes the stored energy between the coils, preventing any single coil from taking a disproportionate amount of energy which could otherwise result in degradation. The operation of these quench heaters is an important part of the testing and qualification procedure for the magnet coils.

This SC magnet is cooled by superfluid helium, since the thermal conductivity of the superfluid state is almost 6 orders of magnitude higher than in the normal state; in addition, the specific latent heat of the superfluid helium is higher than in normal liquid helium and this can also be used to extend the magnet operation time.

Safety of the AMS magnet had to be assured in ground handling operations, during launch, on orbit and during landing. All cryogenic volumes, as well as the vacuum tank, are protected by burst discs to prevent excessive pressures building up in any fault conditions. Some of the burst discs have to operate at temperatures below 2 K have been the subject of a special development and testing program. In addition, extra protection is provided to mitigate the effect of a catastrophic loss of vacuum. All parts of the AMS magnet system are subject to a battery of tests to ensure their quality, integrity and their suitability for the mission. Every one of the 14 superconducting coils have been tested before assembly into the final magnet configuration. A special test facility has been constructed which allows the coil to be operated under cryogenic conditions as close as possible to the launch. Tests have also been carried out on prototype burst discs. Discs for protecting the vacuum tank have undergone vibration testing followed by controlled bursts. These tests have shown that the discs are not affected by the levels of vibration encountered during a launch. Further tests have been carried out on discs for protecting the helium vessel, which operate at 1.8 K. These discs have been shown to have extremely good leak tightness against superfluid helium.

Mechanical tests of the qualification magnet were done at various facilities: study of the low frequency non-linear behavior were done on a special slip table set up at the SERMS Laboratory [54], in Italy, while static tests were done at IABG [55], in Germany, using a mechanically high fidelity replica of the AMS-02 experiment.

The main characteristics of the AMS01/02 and Pamela magnetic systems are listed in Table 18.5.

Table 18.5 Space borne magnets

Parameter	AMS-01/02	PAMELA	AMS-02[a]
Type of magnet	Permanent	Permanent	Superconducting
MDR [TV]	0.55	0.80	2.6
Magnetic field [T]	0.12	0.48	0.75
Dipole bending power [Tm^2]	0.12	0.085	0.75
Maximum torque in geomagnetic field [Nm]		0.0021	0.24
Maximum geometrical acceptance [cm^2 sr]	5000	20.5	5000

[a]Not deployed in space

Table 18.6 Space borne magnetic spectrometers

Particle ID	AMS-01	PAMELA	AMS-02
Transition radiation detector	No	No	Yes
Time of flight	Yes	Yes	Yes
Silicon tracker	Yes	Yes	Yes
Ring imaging Cherenkov	Yes	No	Yes
Electromagnetic calorimeter	No	Yes	Yes
Neutron counter	No	Yes	No

18.7.2 Particle Identification

High precision study of primary energetic Cosmic Rays requires reliable particle identification. Similar detectors to the one used at the accelerators have been developed and qualified for space usage. With respect to accelerators, however, the task of identification a given particle against its background is significantly different, since, at accelerators, the goal is mostly the identification of short lived particles, while in space short lived particles are irrelevant while the goal is the identification of stable particles and long lived isotopes.

Table 18.6 compare the properties of AMS01/02 and Pamela spectrometers.

18.7.2.1 Tracking Detectors

Silicon detectors, commonly used as tracking devices in ground-based accelerator experiments, offer the best resolution in terms of position measurement. However, a large scale application of these devices in space was never made before AMS-01 [56] in 1998. The AMS-02 silicon tracker [57] (Fig. 18.18) is composed by double-sided micro-strip sensors similar to those used for the L3 [58] micro-vertex detectors at the Large Electron-Positron collider (LEP) at CERN, but the technology and the assembly procedures were qualified for the operation in space. The silicon detectors were produced at Colibrys, SA Switzerland [59] and FBK-irst, Italy [60]. The silicon detectors are assembled together forming ladders up to 60 cm long: particular care was taken to control the readout noise produced by these large silicon assemblies, both from the point of view of the capacitive noise as well as from the point of view of the number of defects, which was requested to be below 10^{-3}. The tracker consists of 8 planes of silicon sensors providing 10 μm (30 μm) position resolution in the bending (non-bending) plane of the 0.15 T field of the magnet. The detectors measure both crossing position and energy loss of charged cosmic ray particles. The readout strips of the silicon sensors are ac-coupled to the low noise, high dynamic range, radiation hard, front-end readout chip, the version Hdr9A of the original Viking design, via 700 pF capacitor chips [61]. Once the charge is known, the momentum is determined by the coordinate measurements in the silicon, which are used to reconstruct the trajectory in the magnet field.
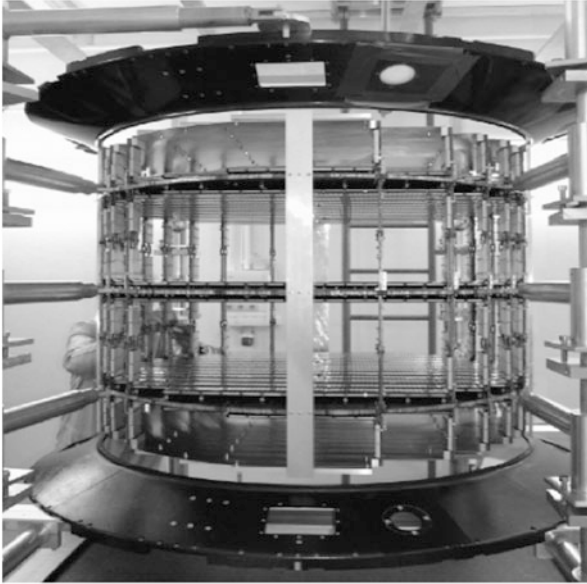
Fig. 18.18 The 8 layers Silicon Tracker of the AMS-02 experiment: the inner planes consists of three double layers of silicon detectors

A similar approach was followed by the PAMELA collaboration. Here the tracking device [62] was based on high accuracy double sided silicon micro-strip detectors organized in 12 cm long silicon ladders, produced by Hamamatsu Photonics [64] while low noise, low power, VLSI VA1 chips were used for the front-end section. The use of low-noise front-end electronics is of great importance since the spatial resolution of the detector is strongly related to its signal-to-noise ratio. The applied position finding algorithm gives a spatial resolution of $2.9 \pm 0.1 \, \mu\text{m}$ [63]. The junction side shows a larger signal-to-noise ratio ($S/N = 49$) and a better spatial resolution. For this reason this side was used to measure the position along the bending view.

18.7.2.2   Time of Flight Detector

The Time-of-Flight (ToF) measurement is typically associated with the experiment trigger, and, in case of compact magnetic spectrometers, these detectors operates in presence of significant magnetic fields. Figure 18.19 show a schematics of the AMS-02 [65] ToF system, the largest of such systems built to date for space operation. This design follows the experience gained with the AMS-01 detector [66], modified to take into account the different conditions in AMS-02, in particular the stronger stray magnetic field at the photomultiplier tubes (PMTs) which can reach several hundred of G. Each scintillating paddle is instrumented with two PMTs at each
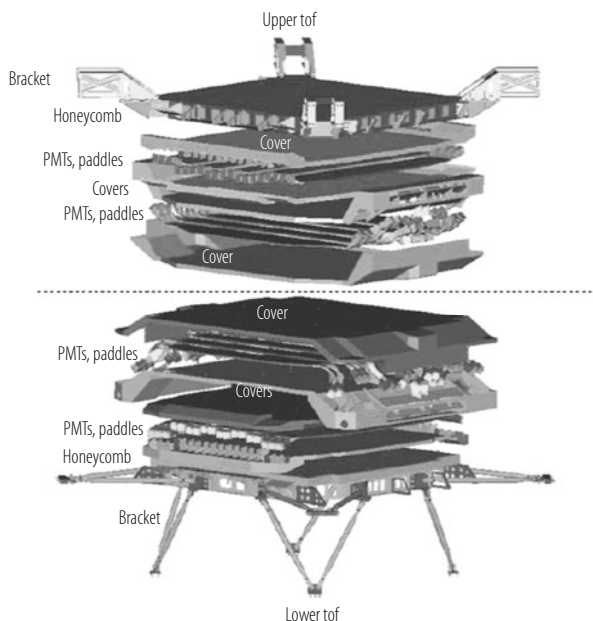
Fig. 18.19 Exploded view of the AMS02 ToF system

end. The time resolution needs to satisfy the physics requirements is 160 ps. The scintillator paddles are 1 cm thick, a compromise between minimum thickness and the light output needed to reach this resolution. Downward going charged particles are distinguished from upward going at the level of 10^9. The system measures the energy loss by a charged particle (to first order proportional to the square of the particle charge) with a resolution sufficient to distinguish nuclei up to charge $Z \sim 20$. Taking into account the attenuation along the counters and the need to have a good measurement of singly charge particles, a dynamic range of more than 10,000 in the measurement of the pulse height is required.

Each paddle is encased in a mechanically robust and light-tight cover and the support structure conforms to the NASA specifications concerning resistance to load and vibrations. The electronics withstands the highly ionizing low Earth orbit environment. Moreover the system guarantees redundancy, with two PMTs on each end of the paddles and double redundant electronics. The system can operate in vacuum over the temperature range -20 to $+50\,°C$, it has a weight of less than 280 kg and a power consumption, including all electronics, lower than 170 W. System components have been qualified for use in space and have been extensively tested with particle beams.

18.7.2.3 Transition Radiation Detector

Because of their low mass, Transition Radiation Detectors (TRD) are well suited for utilization in primary Cosmic Ray experiments to separate leptons (electrons) from hadrons (protons) up to hundreds of GeV of energy. The principle of the TRD is very well understood and these detectors are used in large particle physics experiments like ATLAS [67] and ALICE [68] at CERN, and HERA-B at DESY [69]. However, $TRDs$ are gas based detectors and the new challenge is to operate such a large gas detector safely and reliably in space. This has been achieved in the design and construction of the large AMS-02 TRD [70]. The TR photons are detected in straw tubes, filled with a $Xe:CO_2$ (80%:20%) gas mixture and operated at 1600 V. With a probability of about 50% TR photons are produced in the radiator, 20 mm thick fleece located above each straw layer. Figure 18.20 shows the TRD on top of the magnet vacuum case. The gas tightness of the straw modules is the most critical design issue. The available supplies of gas, 49.5 kg of Xe and 4.5 kg of CO_2, will have to last for 3 years of operation. Using as standard conditions 1 bar and 298 K, this corresponds to 8420 l of Xe and 2530 l of CO_2. The CO_2 leak rate for one meter of straw-tube was measured to be $0.23 \cdot 10^{-6}$ l mbar/s with the TRD gas $Xe:CO_2$ 80:20 mixture. This leak rate is attributed to diffusion through the straw walls. It corresponds to $1.85 \cdot 10^{-5}$ l mbar/s per module-meter or $9.3 \cdot 10^{-3}$ l mbar/s for the full TRD (500 module meters). A single polycarbonate end piece has a CO_2 leak rate of $0.9 \cdot 10^{-5}$ l mbar/s, for all 328*2 end pieces this totals to $5.9 \cdot 10^{-3}$ l mbar/s. Summing, the total TRD CO_2 leak rate of $1.5 \cdot 10^{-2}$ l mbar/s would correspond to a loss of CO_2 over 3 years of 287 l or a safety factor of 8.8 with respect to the CO_2 supply. This low leak rate has been verified on the completely integrated detector, which could then operate in space for about 26 years. Fabricated TRD modules are accepted if they have a leak rate better than a factor 4 with respect to the overall detector limit. This can only be assured by testing each of the 5248
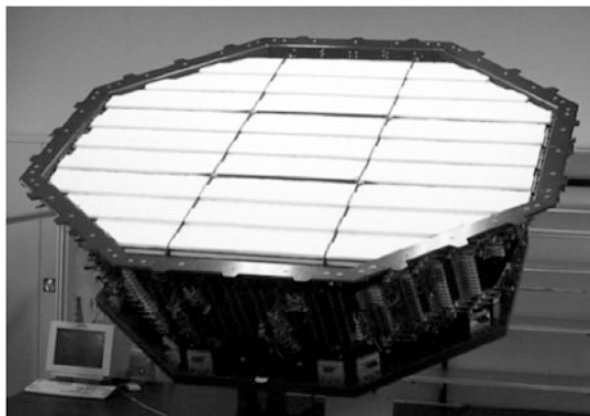

Fig. 18.20 The AMS02 Transition Radiation Detector (TRD) system

straws individually before producing a module [70]. The optimized AMS-02 TRD design with a diameter of 2.2 m and 5248 straw tubes arranged in 20 layers weighs less than 500 kg.

The thermal stability of the TRD is essential for the performance of the detector as temperature variations change the gas density and hence the gas gain. To keep these variations below the 5% level, comparable to other module to module inter-calibration uncertainties, temperature gradients within the TRD should not exceed $\pm 1\,°C$. To keep the spatial and temporal orbit temperature gradient below $1\,°C$ the TRD will be fully covered in multi-layer-insulation (MLI), including the front end electronics. Thermal simulations for orbit parameters which will give the highest TRD temperature swing have been done and prove the effectiveness of this approach. Nonetheless, this has been backed up by a full scale thermal vacuum test in the large volume space simulator at $ESA\ ESTEC$, Holland.

18.7.2.4   Ring Cherenkov Imaging Detector

Cherenkov light is very useful in measuring the velocity and the charge of particles up to tens of GeV of energy, providing a precise measurement to be used together with the momentum determination provided by the spectrometer to identify the different isotopes in the CR flux. The mass of a particle, m, is related to its momentum, p, and velocity, β, through the expression $m = (p/\beta)\sqrt{(1 - \beta^2)}$ and its determination is based on the measurement of both quantities. In the AMS spectrometer, the momentum is determined from the information provided by the Silicon Tracker with a relative accuracy of 2% over a wide range of momenta. This entails an error of the same order on the mass of the particle if the velocity is measured with a relative accuracy of about 1 per mil: this is achieved by fitting the shape of the Cherenkov rings measured on the focal plane by high granularity ($4 \times 4\,mm^2$) pixel photomultipliers located on the focal plane. For this purpose a Ring Imaging Cherenkov Detector (RICH) [71] has been designed with a large geometrical acceptance to operate in the environmental conditions of the outer space. The velocity is determined from the measurement of the opening angle of the Cherenkov cone produced within a radiator layer and the number of detected photons will provide an independent estimation of the charge of the incoming particle.

The measured distribution of charges in the beam is shown in Fig. 18.21 where the structure of individual ion peaks up to $Z = 26$ (Fe) is clearly visible (protons have been suppressed). This spectrum has been fitted to a sum of Gaussian distributions and from their widths we have estimated the charge resolution for each of the ions.
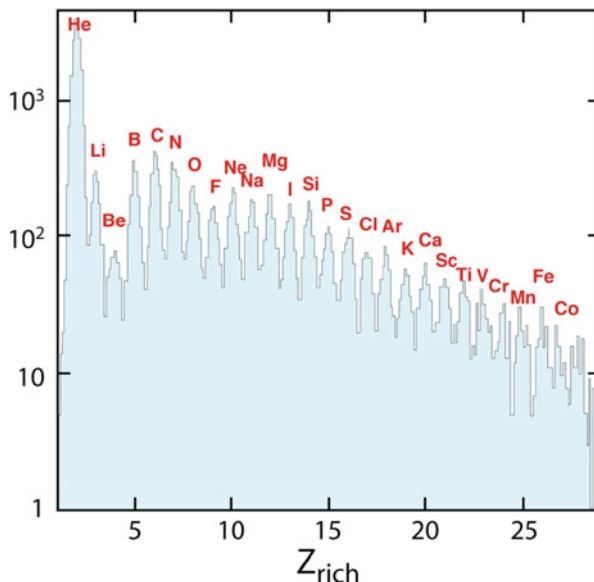
Fig. 18.21 Charge separation of the AMS02 Ring Imaging Cerenkov Detector (RICH) system

18.7.2.5 Electromagnetic Calorimeters

Protons and electrons dominate the positively and negatively charged components of CR, respectively. The main task of the calorimeter is helping the magnetic spectrometer to identify positrons and antiprotons from like-charged backgrounds which are significantly more abundant. Positrons must be identified from a background of protons that increases from about 10^3 times the positron component at 1 GeV/c to $5 \cdot 10^3$ times at 10 GeV/c, and antiprotons from a background of electrons that decreases from $5 \cdot 10^3$ times the antiproton component at 1 GeV/c to less than 10^2 times above 10 GeV/c.

The Electromagnetic Calorimeter ($ECAL$) of the AMS-02 experiment is a fine grained lead-scintillating fiber sampling calorimeter with a thickness corresponding to about 17 radiation lengths [72, 73]. This configuration allows precise, three-dimensional imaging of the longitudinal and lateral shower development, providing at the same time high ($>10^6$) electron/hadron discrimination in combination with the other AMS-02 detectors and good energy resolution, in the range ~ 1 to ~ 1000 GeV when the maximum of the e.m. shower is still within the calorimeter. The $ECAL$ also provides a standalone photon trigger capability to AMS. The mechanical assembly has met the challenges of supporting the intrinsically dense calorimeter during launch and landing with minimum weight. The light collection system and electronics are optimized for the calorimeter to measure electromagnetic particles over a wide energy range, from GeV up to TeV.
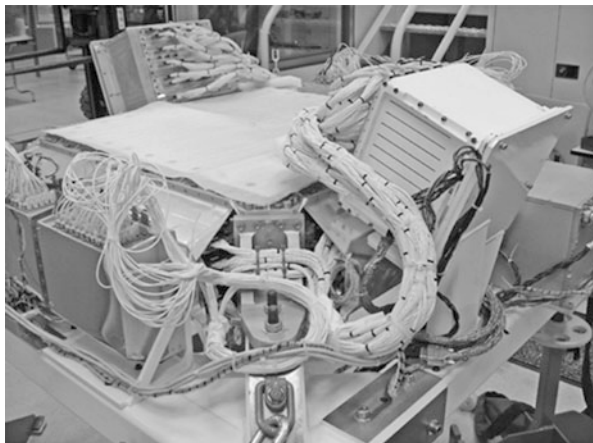
Fig. 18.22 The AMS02 Electromagnetic Calorimeter (ECAL) system

The calorimeter has a total weight of 496 kg. The ECAL mechanical assembly, shown in Fig. 18.22, supports the calorimeter, PMTs and attached electronics. It is designed to minimum weight with a first resonance frequency above 50 Hz, a capability to withstand accelerations up to 14 g in any direction and thermal insulation limiting the gradients (the external temperature ranges from -40 to $+50\,°C$).

The PAMELA ECAL system is a sampling electromagnetic calorimeter comprising 44 single-sided silicon sensor planes (380 μm thick) interleaved with 22 plates of tungsten absorber [74]. Each tungsten layer has a thickness of 0.26 cm, which corresponds to 0.74 X_0 (radiation lengths), giving a total depth of 16.3 X_0 (0.6 nuclear interaction lengths). Each tungsten plate is sandwiched between two printed circuit boards upon which the silicon detectors, front-end electronics and ADCs are mounted. The $(8 \times 8)\,cm^2$ silicon detectors are segmented into 32 read-out strips with a pitch of 2.4 mm. The silicon detectors are arranged in a 3×3 matrix and each of the 32 strips is bonded to the corresponding strip on the other two detectors in the same row (or column), thereby forming 24 cm long read-out strips. The orientation of the strips of two consecutive layers is orthogonal and therefore provides two-dimensional spatial information (*views*). Figure 18.23 shows the calorimeter prior to integration with the other PAMELA detectors.

More recently other space experiments based on fine grained calorimeters have been developed and are operating in space to study the spectrum of high energy electrons and positrons: CALET [75] on the Japanese segment of the ISS and Dampe [76] on a Chinese satellite.
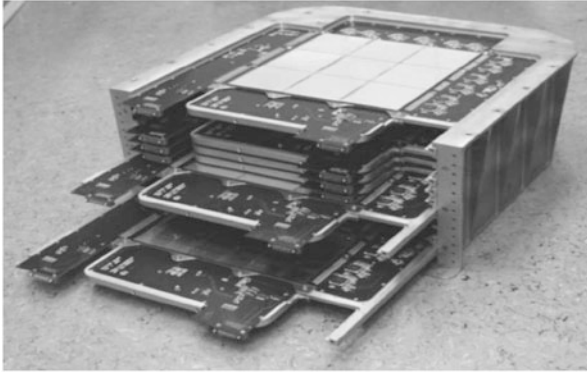
Fig. 18.23 The PAMELA electromagnetic calorimeter. The device is approximately 20 cm tall and the active silicon layer is about $24 \times 24 \, \text{cm}^2$. Some of the detecting planes are seen partially, or fully, inserted

18.8 Gamma Rays Detectors

During the last 30 years astrophysicists have discovered the high energy sky, namely sources emitting gamma rays with energy exceeding 1 MeV. The first space borne detector detecting MeV gamma rays were SAS-2 [77] and COS-B [78], followed by the EGRET instrument [79] which extended the energy range to hundreds of MeV with the Compton Gamma-Ray Observatory (CGRO) [80]. More recently Agile [44] and Fermi [45, 46] extended the energy reach to the GeV and hundreds of GeV scale, respectively, closing the gap with the ground based Cherenkov detectors operating from hundreds GeV to tens of TeV.

At these energies the quantized nature of photons is obvious and optical focusing is not anymore possible: high-energy gamma-rays cannot be reflected or refracted and they are detected by their conversion into an e^+e^- pair using techniques developed in nuclear and particle physics. Since both the gamma rays incoming direction and the energy are important informations, the instrument used are a combination of tracking and calorimetric detectors.

EGRET performed the first all-sky survey above 50 MeV and made breakthrough observations of high energy γ-ray blazars, pulsars, delayed emission from Gamma Ray Bursts ($GRBs$), high-energy solar flares, and diffuse radiation from our Galaxy and beyond that have all changed our view of the high-energy Universe. The EGRET instrument (Fig. 18.24), however, was based on detector technologies developed in the 80's: the tracking was provided by a streak chamber while the energy was measured with crystal based NaI calorimeter. In order to eliminate the background due to the charged CRs, about 10^5 times more frequent, the whole instrument was surrounded by a monolithic anti-coincidence counter. This design had two main limitations. First the limited operation time since the tracking device based on a consumable, the gas mixture. Second at increasing photon energy the anti
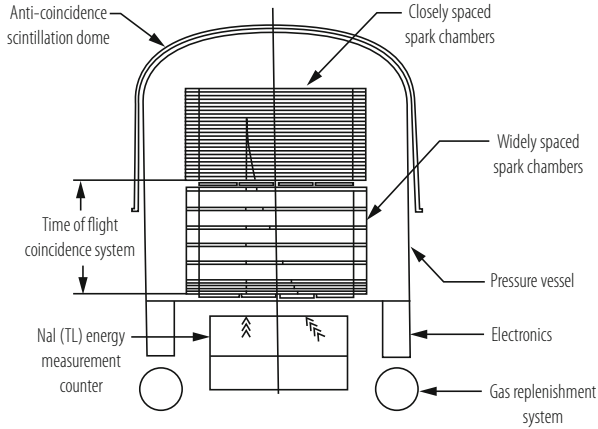
Fig. 18.24 Schematic view of the Energetic Gamma Ray Experiment Telescope (EGRET) on the Compton Gamma Ray Observatory (CGRO)

coincidence system was making the instrument increasingly inefficient due to back scattered particles created in the calorimetric section.

The follow up missions of EGRET, AGILE and Fermi, were based on modern technologies: in these payloads tracking is provided by solid state, imaging calorimeters based on silicon detectors, while the veto system is segmented in several sub elements suitably interconnected within the trigger electronics.

AGILE is a small mission of the Italian Space Agency (ASI), which was launched in April 23rd, 2007. The detector consists on an imaging silicon calorimeter, followed by a thin crystal calorimeter and covered by a coded mask layer to image hard X-rays sources. Its main parameters are listed in Table 18.7.

The Large Area Telescope (LAT) on the Fermi Gamma-ray Space Telescope (Fermi), see Fig. 18.25, formerly the Gamma-ray Large Area Space Telescope (GLAST), was launched by NASA on June 11th, 2008. The LAT is a pair-conversion, high granularity, silicon based imaging telescope made of 16 adjacent towers, followed by an electromagnetic crystal calorimeter. Some of the design choices of Fermi are similar to AGILE, although the detector geometric factor is much larger: each of the 16 Fermi imaging calorimetric towers is equivalent to the whole area of the AGILE detector. In addition the crystal calorimeter section of Fermi is much thicker, providing a much better energy determination. Table 18.8 shows the parameters of the Large Area Telescope instrument.

The self-triggering capability of the LAT tracker is an important new feature of the LAT design made possible by the choice of silicon-strip detectors, which do not require an external trigger, for the active elements [45, 46]. This feature is of essence for the detection of gamma rays in space. In addition, all of the LAT instrument subsystems utilize technologies that do not use consumables such as gas. Upon triggering, the DAQ initiates the read out of these 3 subsystems and utilizes on-board event processing to reduce the rate of events transmitted to ground to a rate

Table 18.7 Agile instrument parameters

Parameter	Value or range
Gamma-ray imaging detector (GRID)	
Energy range	30 MeV–50 GeV
Field of view	~ 2.5 sr
Flux sensitivity ($E > 100$ MeV, 5σ in 10^6 s)	$3 \cdot 10^7$ ph cm^{-2} s^{-1}
Angular resolution	
At 100 MeV (68% cont. radius)	3.5°
At 400 MeV (68% cont. radius)	1.2°
Source location accuracy (high Gal. lat., 90% C.L.)	15 arcmin
Energy resolution (at 400 MeV)	$\Delta E/E \sim 1$
Absolute time resolution	2 μs
Deadtime	$\sim$100–200 μs
Mini-calorimeter	
Energy range	0.35–50 MeV
Energy resolution (at 1.3 MeV)	13% FWHM
Absolute time resolution	$\sim$3 μs
Deadtime (for each of the 30 CsI bars)	$\sim$20 μs
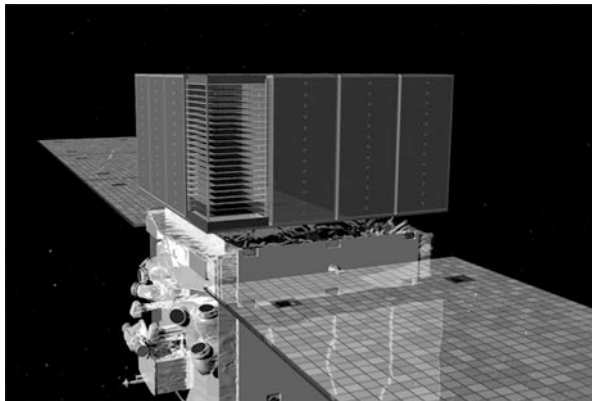
Fig. 18.25 The Fermi Large Area Telescope

compatible with the 1 Mbps average downlink available to the LAT. The on-board processing is optimized for rejecting events triggered by cosmic-ray background particles while maximizing the number of events triggered by gamma-rays, which are transmitted to the ground. Heat produced by the tracker, calorimeter and DAQ electronics is transferred to radiators through heat pipes. The overall aspect ratio of the LAT tracker (height/width) is 0.4, allowing a large field of view and ensuring that nearly all pair conversion events initiated in the tracker will pass into the calorimeter for energy measurement.

Table 18.8 Fermi Large Area Telescope (LAT) parameters [45]

Parameter	Value or range
Energy range	20 MeV–300 GeV
Effective area at normal incidence	9.500 cm^2
Energy resolution (equivalent Gaussian 1σ)	
100 MeV–1 GeV (on axis)	9–15%
1–10 GeV (on axis)	8–9%
10–300 GeV (on-axis)	8.5–18%
>10 GeV (>60° incidence)	≤6%
Single photon angular resolution (space angle)	
On-axis, 68% containment radius	
>10 GeV	≤0.15°
1 GeV	0.6°
100 MeV	3.5°
On-axis, 95% containment radius	<3 × $\theta_{68\%}$
Off-axis containment radius at 55°	<1.7×(on-axis value)
Field of View (FoV)	2.4 sr
Timing accuracy	<10 µs
Event readout time (dead time)	26.5 µs
GRB location accuracy on-board	<10'
GRB notification time to spacecraft	<5 s
Point source location determination	<0.5'
Point source sensitivity (>100 MeV)	3 · 10^{-9} ph cm^{-2} s^{-1}

18.9 Gravitational Waves Detectors

Gravitational Waves (GW) are the analogous of the electromagnetic waves for gravitation. They propagate at the speed of light temporarily deforming the texture of space time. Predicted by Albert Einstein [4] on the basis of his theory of General Relativity, gravitational waves transport energy as gravitational radiation, and have been discovered exactly 100 years later by ground based laser interferometers [3]. They are emitted by massive bodies undergoing acceleration. A two body orbiting system, with masses m_1 and m_2, emits a power P:

$$P = \frac{dE}{dt} = -\frac{32}{5}\frac{G^4}{c^5}\frac{(m_1 m_2)^2 (m_1 + m_2)}{r^5}. \tag{18.2}$$

Emitted power is really small in most gravitating systems. For example, in the case of the Sun–Earth system, it amounts to about 200 W, about $5 \cdot 10^{-25}$ times less that the electromagnetic power emitted by our star. The GW spectrum extends from frequencies corresponding to the inverse of the age of the universe to few hundreds of Hz (Fig. 18.26).

Their detection has only recently been demonstrated on ground but there are solid reasons to believe that the S/N ratio will be much larger for space borne
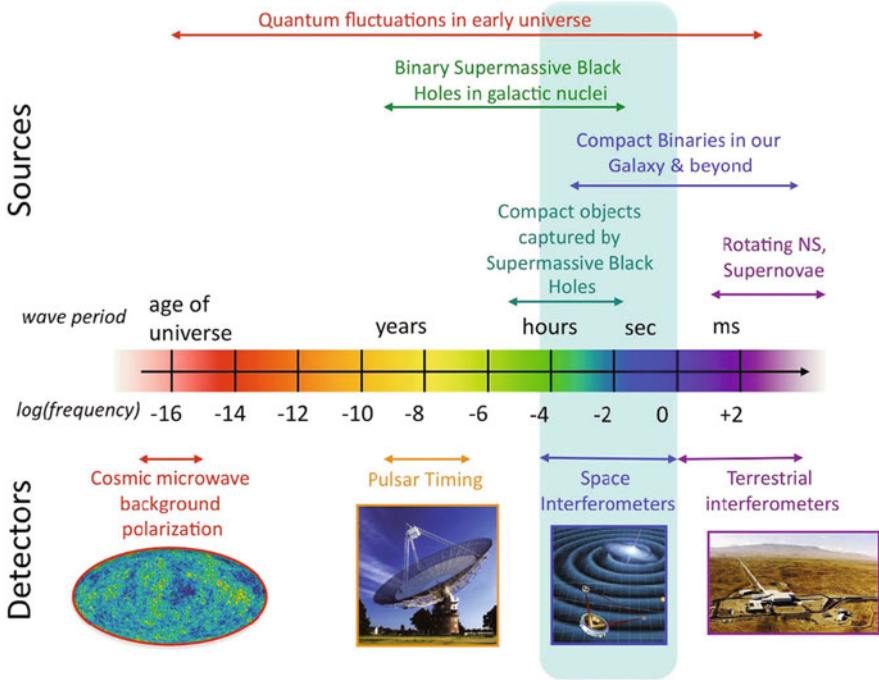
Fig. 18.26 Gravitational wave spectrum and detection techniques

interferometers. LISA is a three-arm space interferometer studied by ESA and NASA up to formulation level for more than 10 years. With the success of the LISA Pathfinder experiment [8], ESA is on track to develop LISA [9] which could be operational towards the beginning of the 30's and detect signals coming from supermassive black-hole mergers, compact objects captured by supermassive black holes and compact binaries (Fig. 18.27).

Once deployed, LISA would measure (a) the orbital period of the binary system, (b) the chirp mass $M = \frac{(m_1 m_2)^{3/5}}{(m_1 + m_2)^{1/5}}$, discriminating between white dwarf, neutron star and black hole binaries and determining the distance for most binary sources with an accuracies better than 1%.

18.9.1 Space-Borne GW Detectors

Measurement of space-time curvature using light beams requires an emitter and a receiver which are perfectly free falling. In flat space-time, the length of proper time between two light-wave crests is the same for the emitter and for the receiver. GW curvature gives oscillating relative *acceleration* to local inertial frames if wave-
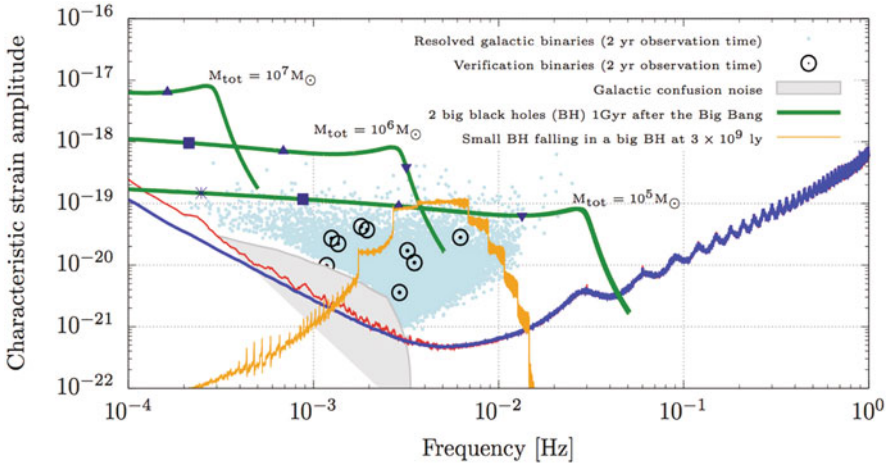
Fig. 18.27 LISA sensitivity to gravitational waves

front is used as a reference: it follows that the receiver sees frequency oscillating. Acceleration of receiver and/or emitter relative to their respective inertial frame produces the same effect of a curvature and should be carefully avoided.

In order to detect gravitational waves via the slowly-oscillating (T up to hours), relative motion they impose onto far apart free bodies, one needs (a) an instrument to detect tiny oscillations, of the size on atom peak-to-peak, ensuring (b) that only gravitational waves can put your test-bodies into oscillation and (c) eliminating all other forces above the weight of a bacteria.

The motion detector (a) is provided by a laser interferometer, as for ground based GW detectors, detecting relative velocities by measuring the Doppler effect through the interferometric pattern variation. Using very stable laser light one can reach the accuracy of 1 atom size in 1 h.

The free falling bodies (b) cannot be touched or supported, at least in an ordinary way. They must be shielded against all other forces (c), in particular, one needs to suppress gravity of the Earth (and of the Sun). The gravity force can be turned off by falling with it, a condition achievable for long periods only on an orbiting satellite. For all other forces, the satellite body would neutralize solar radiation and plasma pressure, actively and precisely following the test mass inertial motion. In order to ensure non contacting (drag-free) behavior, the spacecraft position relative to the test mass is measured by a local interferometer, and it is kept centered on the test mass by acting on micro-Newton thrusters.

The specifications of the LISA GW interferometer design are

- LISA
    - 3 arms, each 5 Mkm
    - $10\,pm/\sqrt{Hz}$ single-link interferometry @1 mHz

- Forces (per unit mass) on test masses $< 3\,fm/(s^2\sqrt{Hz})$ @ 0.1 mHz
- 3 non-contacting ("drag-free") satellites

A basic concept of LISA is that the satellites follow independent heliocentric orbits and no formation keeping is needed. In addition the three satellites constellation rotates with respect to the fixed stars providing gravitational waves source location. In the case of the LISA instrument, the implementation of the requirements (a)–(c) is provided by the following main elements:

- the Gravitational Reference Sensor (GRS) with the test mass (also called Inertial Sensor): the GRS is drag-free along sensitive direction, while the other degrees of freedom are controlled via electrostatic forces through a 3–4 mm clearance between test mass and electrodes (Fig. 18.28);
- the Optical Bench with the complete interferometry: it carries all needed interferometry on a monolithic ultra-stable structure obtained by silica hydroxyl bonding (Fig. 18.29);
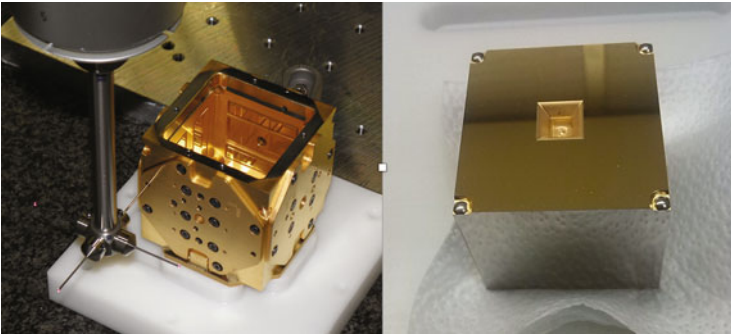- a telescope allowing to exchange light with other satellites.

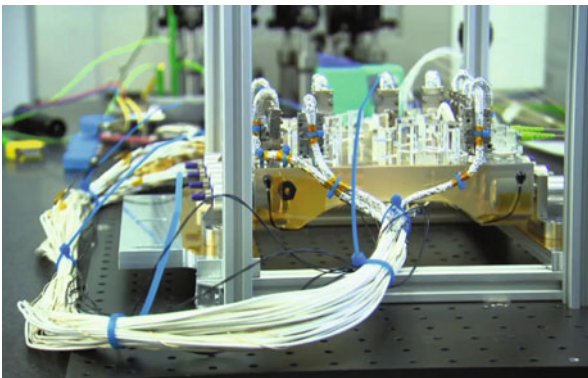**Fig. 18.28** The GRS; left: reference mass housing, right: reference mass

Fig. 18.29 LISA-pathfinder optical bench

18.9.2   LISA Pathfinder

In order to test in space most of the techniques needed for a LISA class space interferometer, the LISA Pathfinder mission has been built, launched in December 3rd 2015 and successfully operated in space during about 8 months, starting from March 1st 2016.

The LISA Pathfinder is based on squeezing of one arm of the final interferometer to within a $O(1)$ m optical bench. This was implemented by removing the long-arm interferometer and replacing the long-arm laser beam reference with a second (quasi-) free test mass. In this miniature implementation of one LISA arm two Au-Pt test masses and two interferometers were placed on the same optical bench. The two masses were not contacting the satellite but the second test mass was forced to follow the first at very low frequency by electrostatic forces (this is different from LISA).

LISA Pathfinder can be seen as a remotely controlled gravitational laboratory operating in space conditions. The GRS consists in two light test masses ($2\,$kg, 46 mm) with a very high density homogeneity ($<<$ $1\,\mu$m pores), so that the position of the CoG at geometrical center is known within $\pm 2\,\mu$m. It has a very low magnetic susceptibility $\chi = -(2.3 \pm 0.2) \cdot 10^{-5}$ as well as a negligible magnetic moment $< 4\,$nAm^2.

Many subtle physical effects apply unwanted forces to test-bodies [81], such as:

- impact with the few molecules that still surround the bodies in high vacuum [82, 83];
- spontaneous electric fields generated by surrounding bodies;
- fluctuating electrical charge from cosmic rays [84];
- changing gravitation generated by thermal deformation of satellite;
- impact with wandering photons;
- fluctuations of the interplanetary magnetic field;

These effects have been studied over the years in the laboratory, pushing forward knowledge in different fields of physics. The results published by the LISA-PF [8] shows that the mission has been very successful, exceeding the predicted accuracy and demonstrating that sub-femto-g differential accelerometry can be achieved, which is an improvement of orders of magnitude with respect to sensors used in the field of experimental gravitation. LISA-PF results confirm the projected LISA sensitivity to the bulk of GW sources present in our galaxy (blue line in Fig. 18.27): a green light for an ESA LISA class mission which could start operating at the beginning of the 30's.

18.10   Future Space Experiments

During the last 20 years an increasing number of modern experiments devoted to particle physics in space have been developed, providing a wealth of new data about CRs composition, high energy astrophysics and gravitational waves. The success of these programs opens the way to the proposal of new, more ambitious projects, designed to measure more accurately the properties of the cosmic radiation.

The universe contains the most powerful particle accelerators, able to accelerate particles to energies inaccessible to ground based laboratories. However these accelerators are quite inefficient and the differential flux of these energetic particles decreases quickly, typically with the third power of the energy. Above a few TeV for the charged component and few hundred GeV for gamma rays, it becomes impractical to develop space instruments having a sufficiently large geometric aperture. For this reason space scientists are considering experiments where the medium where the particle interactions take place is separated from the detector, similarly to what happens for ground based Cherenkov Telescopes, under water or under ice neutrino detectors or Extremely Energetic Cosmic Rays detector arrays, where Cerenkov and fluorescence light produced in the atmosphere, water or ice, respectively, is measured using photon detectors. In the case of these space experiments the medium could be the atmosphere [85, 86], the Moon surface [87] or the magnetosphere [88]: extremely large sensitivities to rare events can be reached by using our whole planet, the Earth, or its satellite, the Moon, as detecting media observable from space borne detectors, collecting emitted light or radio waves by using suitable instrumentation. Discussing these projects is outside the scope of this chapter, however it is interesting to note here a pattern of development which might in the future drive the development of space borne particle experiments devoted to extremely rare events.

18.11   Balloons Experiments

For nearly 40 years, until the mid of the 90's, experiments on stratospheric balloons have been instrumental to study primary CR composition. The advantage of balloons experiments over space experiment is a much lower cost, in the range of 10 M€/mission or less. The main disadvantage is the limited duration of the mission: in the early days it was limited to a day or two, while with the advent of circumpolar flights, the duration has increased to nearly a month/mission. NASA is developing a pressurized balloons technology which would allow for Ultra Long Duration Balloon missions (ULDB) [89, 90] which would reach several months of operation at stratospheric altitudes. In the meantime balloons demonstrated the ability to operate payloads weighting in excess of 1 t, powered by solar panels. It is quite clear that stratospheric balloons missions will be complementary and may become competitive to space missions, in particular when they will last for

several months close to the top of the atmosphere. Most considerations concerning detector developments are quite similar to what has been discussed for space missions: experiments must operate at extreme temperature conditions, withstand shocks, minimize weight and power consumption. Balloons payloads operates in an atmospheric environment, although very rarefied: thermal properties and design should be optimized taking into account also the convective contribution to heat transfer.

References

1. Hess, V., *Über Beobachtungen der durchdringenden Strahlung bei Sieben Freiballonfahrten*, Phys. Z. 13 (1912) 1084.
2. Van Allen, J.A., Ludwig, G.H., Ray, E.C., McIlwain, C.E., *Observations of high intensity radiation by satellites 1958 Alpha and Gamma*, Jet Propulsion 28 (1958) 588–592.
3. Abbott, B. P. et al., *Observation of Gravitational Waves from a Binary Black Hole Merger*, Phys. Rev. Lett. 116 (2016) 061102.
4. Einstein, A.,*Die Feldgleichungen der Gravitation*, Sitzungsberichte der Preussischen Akademie der Wissenschaften zu Berlin, 844–847 (1915).
5. Weber, J., *Gravitational-Wave-Detector Events*, Phys. Rev. Lett. 20 (1968) 1307.
6. Barish, B. C., Weiss, R., *LIGO and the Detection of Gravitational Waves*, Physics Today. 52 (1999) 10.
7. Acernese F. et al., *Advanced Virgo: a second-generation interferometric gravitational wave detector*, Classical and Quantum Gravity, Volume 32, Number 2 (2014).
8. Armano, M. et al., *Sub-Femto-g Free Fall for Space-Based Gravitational Wave Observatories: LISA Pathfinder Results*, P.R.L 116 (2016) 231101.
9. LISA Consortium, *LISA: Laser Interferometer Space Antena*, 20 January 2017.
10. Visentine, J.T. (ed.), *Atomic Oxygen Effects Measurements for Shuttle Missions STS-8 and 41-G*, Vols. I-III, NASA TM-100459 (1988).
11. Leger, L.J., Visentine J.T., Kuminecz, J.F., *Low Earth Orbit Oxygen Effects on Surfaces*, AIAA 22nd Aerospace Sciences Meeting, Reno, NV, Jan. 9–12, 1984.
12. Wertz, J.R., Larson, W.J. (eds.), *Space Mission Analysis and Design*, Microcosm Press and Kluwer Academic Publisher (1999).
13. Gussenhoven, M.S., Hardy, D.A., Rich, F., Burke, W.J., Yeh, H.C., *High Level Spacecraft, Charging in the Low-Altitude Polar Auroral Environment*, J. Geophys. Res. 90 (1985) 11009.
14. Fennel, J.F., Koons, H.C., Leung, M.S., Mizera, P.F., *A Review of SCATHA Satellite Results: Charging and Discharging*, ESA SP-198, Noordwijk, The Netherlands (1983).
15. Purvis, C.K., Garrett, H.B., Witthlesey, A.C., Stevens, N.J., *Design Guidelines for Assessing and Controlling Spacecraft Charging Effects*, NASA Technical Paper 2361 (1984).
16. Vampola, A.L., *The Nature of Bulk Charging and Its Mitigation in Spacecraft Design*, paper presented at WESCON, Anaheim, CA, Oct. 22–24, 1996.
17. Walt, M., *Introduction to Geomagnetically Trapped Radiation*, Cambridge University Press (1994).
18. McIlwain, C.E., *Coordinates for Mapping the Distribution of Magnetically Trapped Particles*, J. Geophys. Res. 66 (1961) 3681–3691.
19. Cervelli, F., et al., *The space qualified read-out electronics for the e.m. calorimeter (ECAL) of the AMS-02 experiment*, IEEE, TNS-00184-2009.
20. National Space Science Data Center web site: http://nssdc.gsfc.nasa.gov/.
21. Alpat, B., et al., *A pulsed nanosecond IR laser diode system to automatically test the Single Event Effects in Laboratory*, Nucl. Instrum. Meth. A 485 (2002) 183–187.

22. see Chapter 3 on *Managing Space Radiation Risk in the New Era of Space Exploration*, Committee on the Evaluation of Radiation Shielding for Space Exploration of the Aeronautics and Space Engineering Board (National Research Council, USA), National Academies Press, Washington DC (2008), ISBN 9780309113830.

23. SPENVIS, *ESA's SPace ENVironment Information System* (2018), available at https://www.spenvis.oma.be/.

24. OMERE software (2018), *Outil de Modèlisation de l'Environnement Radiatif Externe*, the code is developed by TRAD with the support of the CNES and is available at http://www.trad.fr/en/space/omere-sotftware/.

25. SR-NIEL Calculator: *Screened Relativistic (SR) Treatment for Calculating the Displacement Damage and Nuclear Stopping Powers for Electrons, Protons, Light- and Heavy- Ions in Materials* by Boschini, M.J., Rancoita, P.-G. and Tacconi, M., current version 3.9.3 (October 2017) is available at http://www.sr-niel.org/; the treatment can be comprehensively found in Chapters 2, 7 and 11 of [26].

26. Leroy, C. and Rancoita, P.-G., *Principles of Radiation Interaction in Matter and Detection* 4th Edition, World Scientific (Singapore) 2016, ISBN 9789814603188.

27. GRAS *(Geant4 Radiation Analysis for Space)* code is available at ESA website upon registration; the original article is by Santin, G., Ivanchenko, V., Evans, H., Nieminen, P. and Daly, E., IEEE Trans. Nucl. Sci. 52, Issue 6, 2005, pp 2294–2299.

28. MULASSIS - *MUlti-LAyered Shielding SImulation Software, available at ESA website*: the original article is by Lei, F., Truscott, R.R., Dyer, C.S., Quaghebeur, B., Heynderickx, D., Nieminen, P., Evans, H. and Daly, E., IEEE Transactions on Nuclear Science Vol 49 No 6 (2002) P2788–2793.

29. Streitmatter, R.E., *ISOMAX: A Balloon-borne Instrument to Study Berlyllium and Other Light Isotopes in the Cosmic Radiation*, Proc. 23th Int. Cosmic Ray Conf., Calgary 1993.

30. Mitchell, J.W., et al., *(IMAX) Isotope Matter-Antimatter Experiment*, Proc. 23rd Int. Cosmic Ray Conf., Calgary 1993, Vol. 1, p. 519.

31. Carlson, P., Francke, T., Suffert, M., Weber, N., *A RICH counter for antimatter and isotope identification in the cosmic radiation*, Proc. 23th Int. Cosmic Ray Conf., Calgary 1993, Vol. 2, p. 504.

32. Yamamoto, A., et al., *Balloon-Borne Experiment with a Superconducting Solenoidal Magnet Spectrometer*, Adv. Space Res. 14(2) (1994) 75–87.

33. Barwick, S.W., et al., *The High-Energy Antimatter Telescope (HEAT): an instrument for the study of cosmic-ray positrons*, Nucl. Instrum. Meth. A 400 (1997) 34–52.

34. Beatty, J.J., et al., *Cosmic Ray Energetics And Mass (CREAM): A Detector for Cosmic Rays near the Knee*, Proc. 26th Int. Cosmic Ray Conf., Salt Lake City 1999, Vol. 5, pp. 61–64.

35. Isbert, J., et al., *ATIC, a Balloon Borne Calorimeter for Cosmic Ray Measurements*, Proc. 10th Int. Conf. Calorimetry in Particle Physics, Pasadena, CA, March 25, 2002, pp. 89–94.

36. Boyle, P., et al., *Cosmic Ray Energy Spectra of Primary Nuclei from Oxygen to Iron: Results from the TRACER 2003 LDB Flight*, 30th Int. Cosmic Ray Conf., Merida, Mexico (2007).

37. Yoshimura, K., et al., *The First BESS-Polar Flight over Antarctica*, Proc. 25th Int. Symp. Space Technology and Science, Kanazawa, Japan (2006), pp. 1132–1137.

38. Seo, E.S., et al., *CREAM: 70 days of flight from 2 launches in Antarctica*, Advances in Space Research 42 (2008) 1656–1663.

39. Baker, D.N., Mason, G.M., Figueroa, O., Colon, G., Watzin, J.G., Aleman, R.M., *An Overview of the Solar, Anomalous, and Magnetospheric Particle Explorer (SAMPEX) Mission*, IEEE Trans. Geosci. Remote Sens. 31 (1993) 531–541.

40. ESA's Report to the 30th COSPAR Meeting, Hamburg, Germany, July 1994, European Space Agency, Paris, (1992) 47–57.

41. Ahlen, S.P., et al., *An Antimatter spectrometer in space*, Nucl. Instrum. Meth. A 350 (1994) 351–367.

42. AMS Collaboration, Aguilar, M., et al., *The Anti Matter Spectrometer (AMS-02): A particle physics detector in space*, Nucl. Phys. Proc. Suppl. 166 (2007) 19–29.

43. Bonvicini, V., et al., *The PAMELA experiment in space*, Nucl. Instrum. Meth. A 461 (2001) 262–268.
44. Tavani, M., et al., Astron. Astrophys. 502 (2009) 995.
45. Atwood, W.B., et al., *The Large Area Telescope on the Fermi Gamma-ray Space Telescope Mission*, Astrophys. J. 697 (2009) 1071–1102.
46. Meegan, C., et al., *The Fermi Gamma-Ray Burst Monitor*, Astrophys. J. 702 (2009) 791–804.
47. AMS Collaboration, Aguilar, M., et al., *The Alpha Magnetic Spectrometer (AMS) on the International Space Station. Part I: Results from the Testflight on the Space Shuttle*, Physics Reports 366 (2002) 331–405.
48. Institute of Electrical Engineering, IEE, Chinese Academy of Sciences, 100080 Beijing, China.
49. Chinese Academy of Launching Vehicle Technology, CALT, 100076 Beijing, China.
50. CMS Physics, Technical Design Report, Volume I: CERN-LHCC-2006-001, Feb. 2, 2006.
51. ATLAS detector and physics performance, Technical Design Report, Volume I, May 25, 1999.
52. Jones, W. V., *Astromag - Particle astrophysics magnet facility for Space Station Freedom*, IAF, 40th Int. Astronautical Congress, Malaga, Spain, Oct. 7–13, 1989.
53. Blau, B., et al., Grav. Cosmol. Suppl. 5 (2000) 1; IEEE Trans. Appl. Supercond. 12 (2002) 349.
54. SERMS, Via Pentima 4, 05100 Terni, Italy; Bertucci, B., *The S.E.R.M.S. laboratory. A research and test facility for space payloads and instrumentation*, Memorie della Societa Astronomica Italiana 79 (2008) 818.
55. IABG mbH, Einsteinstrasse 20, 85521 Ottobrunn, Germany.
56. Battiston, R., *A silicon tracker for the antimatter spectrometer on the International Space Station ALPHA*, Proc. 1st Arctic Workshop Future Physics and Accelerators, Saariselka, Finland, Aug. 21–26, 1994, (1994) 138–156; Alcaraz, J., et al., *A silicon microstrip tracker in space: Experience with the AMS silicon tracker on STS-91*, Nuovo Cimento A 112 (1999).
57. Alcaraz, J., et al., *The alpha magnetic spectrometer silicon tracker: Performance results with protons and helium nuclei*, Nucl. Instrum. Meth. A 593 (2008) 376–398, Erratum: *ibid.* 597 (2008) 270.
58. Acciarri, M., et al., *The L3 silicon microvertex detector*, Nucl. Instrum. Meth. A 351 (1994) 300–312.
59. Colibrys (Switzerland) Ltd, Maladière 83, 2000 Neuchâtel, Switzerland.
60. FBK-irst, Via Sommarive, 18, 38050 Povo (Trento), Italy.
61. Toker, O., et al., Nucl. Instrum. Meth. A 340 (1994) 572.
62. Picozza, A., et al., Astroparticle Phys. 27 (2007) 296–315.
63. Straulino, S., et al., *Spatial resolution of double-sided silicon microstrip detectors for the PAMELA apparatus*, Nucl. Instrum. Meth. A 556 (2006) 100–114.
64. 5000, Hirakuchi, Hamakita-ku, Hamamatsu City, Shizuoka Pref., 434-8601, Japan.
65. Bindi, V., et al., *The AMS-02 time of flight system. Final design*, Proc. 28th Int. Cosmic Ray Conf., Tsukuba, Japan, July 31 - Aug. 7, 2003.
66. Baldini, L., *The AMS time-of-flight system*, Proc. 27th Int. Cosmic Ray Conf., Hamburg, Germany, Aug. 7–15, 2001.
67. The ATLAS TRT collaboration, Abat, E., et al., J. Instrum. 3 (2008) P02014.
68. ALICE TRD Collaboration, *The ALICE transition radiation detector*, Nucl. Instrum. Meth. A 502 (2003) 127–132.
69. Saveliev, V., *The HERA-B Transition Radiation Detector*, Nucl. Instrum. Meth. A 408 (1998) 289–295.
70. Siedenburg, T., et al., *A transition radiation detector for AMS*, Nucl. Phys. Proc. Suppl. 113 (2002) 154–158.
71. Casaus, J., et al., *The AMS RICH detector*, Nucl. Phys. Proc. Suppl. 113 (2002) 147–153.
72. Adinolfi, M., et al., *The KLOE electromagnetic calorimeter*, Nucl. Instrum. Meth. A 482 (2002) 364–386.
73. Cadoux, F., et al., *The AMS-02 electromagnetic calorimeter*, Nucl. Phys. Proc. Suppl. 113 (2002) 159–165.
74. Bonvicini, V., et al., *A silicon-tungsten imaging calorimeter for PAMELA*, Proc. 26th Int. Cosmic Ray Conf. (ICRC 99), Salt Lake City, Utah, Aug. 17–25, 1999, Vol. 5, pp. 187–190.

75. Torii S. et al., *Calorimetric electron telescope mission. Search for dark matter and nearby sources*, Nucl. Instr. and Meth. A 630 (2011) 55-7; Torii S. et al., Proc. of 33rd ICRC (2013) 245

76. Chang J et al., *Dark Matter Particle Explorer: The First Chinese Cosmic Ray and Hard γ-ray Detector in Space*, Chin. J. Space Sci. 34 (2014); Chang J et al., *The DArk Matter Particle Explorer mission*, Astropart. Phys. 95 (2017) 6

77. Derdeyn, S.M., Ehrmann, L.H., Fichtel, G.J., Kniffen, D.A., Ross, R.W., Nucl. Instrum. Meth. 98 (1972) 557.

78. Bignami, G.F., et al., Space Sci. Instrum. 1 (1975) 245.

79. Thompson, D.J., et al., Astrophys. J. 415 (1993) L13.

80. Thompson, D.J., et al., Astrophys. J. Suppl. Ser. 86 (1993) 629.

81. Carbone, L. et al., *Thermal gradient-induced forces on geodesic reference masses for LISA*, P.R.L. D76 (2007) 102003

82. Carbone L., et al., *Achieving Geodetic Motion for LISA Test Masses: Ground Testing Results* P.R.L. 91 (2003) 151101; Erratum-ibid. P.R.L. 91 (2003) 179903

83. Cavalleri, A., *Increased Brownian Force Noise from Molecular Impacts in a Constrained Volume*, P.R.L. D103 (2009) 140601

84. Antonucci, E. et al., *Interaction between Stray Electrostatic Fields and a Charged Free-Falling Test Mass*, P.R.L. D108 (2012) 181101

85. G. D'Ali Staiti, G., et al., *EUSO: A space mission searching for extreme energy cosmic rays and neutrinos*, Nucl. Phys. Proc. Suppl. 136 (2004) 415–432.

86. Takahashi, Y., *A Giant natural TPC (500 km)^3 to observe extremely high energy cosmic particles - JEM EUSO telescope on International Space Station*, J. Phys. Conf. Ser. 65 (2007) 012022.

87. Battiston, R., Brunetti, M.T., Cervelli, F., Fidani, C., Menichelli, M., *A Moon-borne electromagnetic calorimeter*, Astrophys. Space Sci. 323(4) (2009) 357–366.

88. Gusev, A.A., et al., *Detector for electron spectrum measurements in TeV region on synchrotron radiation in geomagnetic field*, Proc. 21st Int. Cosmic Ray Conf., Adelaide 1990, Vol. 3, pp. 245–248; Anderhub, H., et al., *Preliminary results from the prototype Synchrotron Radiation Detector on Space Shuttle mission STS-108*, Nucl. Phys. Proc. Suppl. 113 (2002) 166–169.

89. *NASA Stratospheric Balloons Pioneers of Space Exploration and Research*, Report of the Scientific Ballooning Planning Team, Oct. 2005; http://sites.wff.nasa.gov/code820/uldb.html.

90. Wiencke, L., *EUSO-Balloon mission to record extensive air showers from near space*, PoS ICRC 2015, (2016) 631.